

1
2
3
4
5
6
7
8
9
10
11
12
13
14
15
16
17
18
19
20
21

How to process radio occultation data: 1. From time series of frequency residuals to vertical profiles of atmospheric and ionospheric properties

22 Paul Withers^{a,b,*}, L. Moore^b, K. Cahoy^c, I. Beerer^c

23
24
25 ^a*Department of Astronomy, Boston University, 725 Commonwealth Avenue,*
26
27 *Boston, MA 02215, USA*

28
29 ^b*Center for Space Physics, Boston University, 725 Commonwealth Avenue,*
30
31 *Boston, MA 02215, USA*

32
33
34 ^c*Department of Aeronautics and Astronautics, MIT, 77 Massachusetts Avenue,*
35
36 *Cambridge, MA 02139, USA*

37
38
39
40 **Abstract**

41
42
43 Expertise in processing radio occultation observations, which provide vertical pro-
44 files of atmospheric and ionospheric properties from measurements of the frequency
45 of radio signals, is not widespread amongst the planetary science community. In
46 order to increase the population of radio occultation processing experts, which will
47 have positive consequences for this field, here we provide detailed instructions for
48 one critical aspect of radio occultation data processing: how to obtain a series of
49 bending angles as a function of the ray impact parameter from a time series of fre-
50 quency residuals. As developed, this tool is valid only for one-way, single frequency
51 occultations at spherically symmetric objects, and is thus not immediately applica-
52
53
54
55
56
57
58
59
60
61
62
63

1
2
3
4 ble to either two-way occultations, such as those of Mars Express, or occultations
5
6 at oblate objects, such as Jupiter or Saturn. This tool is demonstrated successfully
7
8 on frequency residuals from a Mars Global Surveyor occultation at Mars, and the
9
10 resultant set of bending angles and impact parameters are used to obtain vertical
11
12 profiles of ionospheric electron density, neutral atmospheric number density, mass
13
14 density, pressure, and temperature via the usual Abel transform. The root-mean-
15
16 square difference between electron densities in the ionospheric profile derived herein
17
18 and archived electron densities is $7 \times 10^8 \text{ m}^{-3}$. At the lowest altitudes, temperatures
19
20 in the neutral atmospheric profile derived herein differ from archived neutral tem-
21
22 peratures by less than 0.1 K. Software programs that implement these procedures
23
24 accompany this manuscript and may be used to extract scientifically useful data
25
26 products from lower-level data sets.
27

28
29 *Key words:* Radio occultation, ionosphere, atmosphere, data processing
30
31

32 33 34 35 36 **1 Introduction** 37

38
39
40
41 Radio occultation investigations have been commonplace on planetary sci-
42
43 ence flyby and orbital missions since Mariner 4 reached Mars in 1965 (Kliore
44
45 et al., 1965), with dozens of spacecraft performing radio occultations at many
46
47 planets, satellites, and a comet (Withers, 2010). The application of radio oc-
48
49 cultation investigations to planetary science has been described previously
50
51 by several authors (e.g. Phinney and Anderson, 1968; Fjeldbo et al., 1971;
52
53 Yakovlev, 2002; Kliore et al., 2004; Withers, 2010). These investigations trans-
54
55 mit a radio signal such that it passes close to a solar system object (the “target
56
57

58
59

* Corresponding author

60 *Email address:* withers@bu.edu (Paul Withers).
61
62
63

1
2
3
4 object”) during its journey from the transmitter to the receiver. Refraction of
5
6 the radio signal in the neutral gas and ionospheric plasma around the target
7
8 object affects the frequency of the radio signal. Vertical profiles of the num-
9
10 ber density of neutral gas and the electron density of ionospheric plasma can
11
12 be obtained from time series measurements of the received radio frequency.
13
14 Corresponding profiles of neutral mass density, pressure, and temperature can
15
16 also be obtained. The resultant neutral atmospheric profiles offer better ver-
17
18 tical resolution (sub-km) than most other techniques and are unaffected by
19
20 instrument calibration issues. They are also referenced to an absolute altitude
21
22 scale, unlike the pressure levels that are common to many infrared instru-
23
24 ments, which provides deeper context for studies of atmospheric dynamics.
25
26 In addition, compared to data sets from many other instruments, they have
27
28 high accuracy at relatively high pressures, which enhances studies of tropo-
29
30 spheric climate and, on objects whose surface pressure is not much greater than
31
32 Earth’s, atmosphere-surface interactions. Radio occultation investigations are
33
34 even more valuable for planetary ionospheric studies than for planetary at-
35
36 mospheric studies — indeed, they have provided almost all measurements of
37
38 planetary ionospheres.
39
40
41
42
43
44

45 However, the expertise necessary to obtain useful information about plane-
46
47 tary environments from the recorded frequency measurements has not been
48
49 widely disseminated across the scientific community in the fifty years since
50
51 these skills were first developed. With one exception, merely two institu-
52
53 tions, the NASA Jet Propulsion Laboratory (JPL) and Stanford, have pro-
54
55 vided the Principal Investigators or Team Leaders for every NASA plane-
56
57 tary radio occultation investigation (see list of investigations and personnel
58
59 at <http://nssdc.gsfc.nasa.gov/planetary/> for each mission). The exception oc-
60
61
62
63
64
65

1
2
3
4 curred when Dick French of Wellesley College replaced Arv Kliore of JPL as
5
6 Principal Investigator of the Cassini Radio Science Subsystem some time af-
7
8 ter completion of Cassini’s nominal mission. These two institutions have also
9
10 provided most of the team members with instrumentation, operations, or data
11
12 processing expertise (as opposed to scientific analysis of derived atmospheric
13
14 and ionospheric properties). This localization of expertise was identified as
15
16 a potential concern by Cornell University in the 1970s when Nicholson and
17
18 Muhleman (1978) stated that “such an important experiment should be sub-
19
20 ject to independent confirmation, both to determine the reproducibility of the
21
22 results and to check for systematic errors.” They successfully reproduced the
23
24 reported results of the Mariner 10 radio occultation investigation. This legacy
25
26 at Cornell continues into the present day, with independent analysis of Cassini
27
28 radio occultation measurements at Titan and Saturn (Schinder et al., 2011a,b,
29
30 2012). Expertise also exists in Europe, where groups from Cologne and Munich
31
32 lead radio science investigations on Rosetta, Mars Express, and Venus Express
33
34 (Pätzold et al., 2004; Häusler et al., 2006; Pätzold et al., 2007); Japan, where
35
36 the Sakigake, Nozomi, Selene, and Akatsuki spacecraft carried radio occulta-
37
38 tion investigations (Oyama et al., 2001; Noguchi et al., 2002; Imamura et al.,
39
40 2011, 2012); and China (Hu et al., 2010). Several groups also possess related
41
42 expertise concerning radio occultations of Earth’s atmosphere and ionosphere
43
44 (e.g. Kursinski et al., 1997, 2000; Anthes et al., 2008).
45
46
47
48
49
50

51
52 Consequently, radio occultation investigations are often viewed by the plan-
53
54 etary science community as an esoteric speciality. Hands-on analysis of all
55
56 radio occultation data products that precede the final vertical profiles of neu-
57
58 tral atmospheric and ionospheric properties has been conducted by only a
59
60 small subset of those using these final products. It is clearly detrimental to
61
62
63
64
65

1
2
3
4 the advancement of planetary science for the vast majority of the users of
5 these data sets to have such limited awareness of the preceding data pro-
6 cessing steps. For instance, such users are hard-pressed to critically evaluate
7 whether an unusual feature in the final data products is an exciting scientific
8 discovery or an instrumental glitch. Another consequence is that atmospheric
9 and ionospheric profiles that were not comprehensively archived by the orig-
10 inal investigators are effectively lost, since barely any scientists interested in
11 analyzing these profiles have the skills necessary to recover them. This is not
12 merely a hypothetical concern: the atmospheric and ionospheric profiles ac-
13 quired by missions as significant as Pioneer Venus Orbiter, the Voyagers, and
14 the Viking Orbiters are not archived. Images of some of these profiles may be
15 present, in cramped and cropped formats, in published articles, but today's
16 scientists are unable to work meaningfully with these profiles. If the size of
17 the community capable of obtaining such profiles from raw radio occultation
18 data were to increase, then some of these past data sets could be regenerated
19 and the chances of current and future data sets suffering a similar fate would
20 diminish.

21
22
23
24
25
26
27
28
29
30
31
32
33
34
35
36
37
38
39
40
41
42
43 Our aim in this manuscript is to make this arcane skill more readily accessible
44 to the broader scientific community. Although the theory of how to process
45 radio occultation data has been presented in several publications, it is ex-
46 ceedingly challenging to create a functional radio occultation processing tool
47 from the scientific literature without mentoring from an expert. Many issues
48 important for practical implementation are stated either implicitly or not at
49 all. Here we describe how to implement one of the key steps in the processing
50 of radio occultation data: the determination of vertical profiles of atmospheric
51 properties from time series of "frequency residuals". As will be explained in
52
53
54
55
56
57
58
59
60
61
62
63
64
65

1
2
3
4 more detail in Section 3, the frequency residual is the difference between the
5
6 frequency of the received radio signal and the frequency it would have had
7
8 in the absence of refraction in the atmosphere and ionosphere of the solar
9
10 system object that is the target of the occultation. The frequency residual is
11
12 intimately associated with the number densities of neutral gas and ionospheric
13
14 plasma around the target object. The software programs that were developed
15
16 in the course of writing this manuscript accompany this publication, and we
17
18 hope these programs in the IDL programming language will encourage many
19
20 readers to work more closely with radio occultation data sets.
21
22

23
24 There are many types of radio occultation experiments and here we focus on
25
26 the simplest example: a one-way, single frequency downlink experiment with
27
28 a transmitter that has a stable frequency source and a target object whose
29
30 atmosphere and ionosphere can be assumed to be spherically symmetric. Mars
31
32 Global Surveyor is representative of this type of radio occultation experiment.
33
34 We focus on this simple type because it offers the clearest possible framework
35
36 for establishing and illustrating the practical principles of a radio occultation
37
38 experiment. We discuss the numerous limitations that arise from this deci-
39
40 sion in Section 5. It is hoped that this will be the first of a series of papers
41
42 concerning how to process radio occultation data in which the future papers
43
44 will present more sophisticated tools developed from the present work that
45
46 are suitable for more complex radio occultation experiments.
47
48
49

50
51 Detailed knowledge of the positions and velocities of solar system objects, both
52
53 natural and artificial, as functions of time is required for the interpretation of
54
55 radio occultation observations. The JPL SPICE system provides a remarkably
56
57 straightforward, yet powerful, tool for obtaining and manipulating such infor-
58
59 mation (<http://naif.jpl.nasa.gov>). Our software makes extensive use of SPICE
60
61
62
63

1
2
3
4 and it is painful to imagine how radio occultation data processing would be
5
6 accomplished without a tool like SPICE.
7
8

9
10 Section 2 explains why the angle by which a radio ray is bent is useful. Sec-
11 tion 3 describes how to derive vertical profiles of ray bending angles from
12 time series of frequency residuals. It presents the basic requirements (Sec-
13 tion 3.1), explains how the relativistic Doppler shift alters the radio frequency
14 (Section 3.2), introduces the concept of the frequency residual (Section 3.3),
15 and links the frequency residual to the bending angle (Sections 3.4–3.7). Sec-
16 tion 4 applies this method to a sample of Mars Global Surveyor data from
17 Mars, including the transformation of bending angles into vertical profiles of
18 refractive index, ionospheric electron density, neutral density, pressure, and
19 temperature. These results are validated against archived results. Section 5
20 discusses the many limitations of our method, which is less sophisticated than
21 the state-of-the-art tools used by active flight missions. Section 6 presents the
22 conclusions of this work.
23
24
25
26
27
28
29
30
31
32
33
34
35
36
37
38
39
40

41 **2 Why bending angles are useful**

42
43
44
45 The objective of a radio occultation is to obtain scientifically-useful informa-
46 tion about the environment through which a radio signal has propagated by
47 analysis of properties of that radio signal. The primary environmental prop-
48 erty that is usually determined is the refractive index. In geometric optics, the
49 direction of propagation of a ray depends on the refractive index, n , as follows
50 (Born and Wolf, 1959):
51
52
53
54
55
56
57
58

$$59 \frac{d}{dl} (n\hat{l}) = \nabla n \quad (1)$$

1
2
3
4 Here unit vector \hat{l} is the direction of propagation of the ray. Consequently, the
5
6 path of a radio ray bends as it passes through an atmosphere or ionosphere,
7
8 except for the unlikely case of radio transmission through a medium in which
9
10 the gradient of refractive index is parallel to the direction of propagation. The
11
12 total angle by which a radio ray is bent during its passage through an at-
13
14 mosphere and/or ionosphere depends on the refractivity of the environment
15
16 through which it passes. Under certain assumptions, the dependence of the
17
18 refractive index on radial distance can be obtained from the dependence of
19
20 bending angle on impact parameter. In turn, neutral and plasma densities
21
22 can be found from the refractive index. Hence radial profiles of neutral and
23
24 plasma densities can be obtained from the dependence of bending angle on
25
26 impact parameter. Therefore it would be useful in a radio occultation to de-
27
28 termine the bending angle of radio signals as a function of impact parameter.
29
30 However, the bending angle itself is not directly observable. Hence we outline
31
32 how changes in the frequency of a radio signal, which are readily observable,
33
34 are related to bending angle. That information will be sufficient for the deter-
35
36 mination of radial profiles of neutral and plasma densities, quantities which
37
38 are scientifically useful.
39
40
41
42
43
44
45
46

47 **3 From frequency residuals to bending angles**

48 *3.1 Basic requirements*

49
50
51 Here we describe how to determine the bending experienced by a radio signal
52
53 given information about the frequency of the received radio signal. Our objec-
54
55 tive is to obtain a series of bending angles as a function of impact parameter,
56
57
58
59
60
61
62
63
64
65

1
2
3
4 from which neutral and plasma densities can eventually be determined. We
5 describe the occultation geometry, how the relativistic Doppler shift alters the
6 radio frequency, and how refractive bending of the ray affects the frequency.
7
8
9

10
11 Figure 1 shows the canonical description of the geometry of a radio occulta-
12 tion observation, based on Figure 20 of Fjeldbo et al. (1971). The discussion in
13 Section 3 builds upon the themes and approaches introduced by Fjeldbo et al.
14 (1971), but with the addition of relativistic corrections and explicit instruc-
15 tions on how to calculate the necessary quantities. We use different symbols
16 from those in Fjeldbo et al. (1971) in order to better emphasize aspects of our
17 technique. Table 1 provides a conversion table for these symbols.
18
19
20
21
22
23
24
25
26

27 We use \underline{x}_i to represent the vector position of location i , where i is A (transmit-
28 ter), B (receiver), P (target object), O (defined below), or X (defined below).
29
30 In Figure 1, the radio signal is transmitted from \underline{x}_A at time t_A and received
31 at \underline{x}_B at time t_B . Instead of proceeding directly along the straight line path
32 between the position of the transmitter A at time t_A and the position of the
33 receiver B at time t_B , it moves initially away from the position of the transmit-
34 ter A at time t_A in a straight line at some angle to the anticipated trajectory.
35 It passes through the atmosphere and ionosphere of the target object P and
36 emerges on a final straight line path towards the position of the receiver B at
37 time t_B . Refraction in the atmosphere and ionosphere of the target object has
38 changed the direction of propagation of the radio signal. We call the initial
39 and final straight line paths the two asymptotes of the ray path. The point
40 of closest approach of the radio signal transmitted at time t_A to the target
41 object P is \underline{x}_O , the time at which this radio signal is at this position is t_O ,
42 and the two asymptotes of this ray path intersect at position \underline{x}_X . Note that
43
44
45
46
47
48
49
50
51
52
53
54
55
56
57
58
59
60
61 $\underline{x}_O \neq \underline{x}_X$.
62
63
64
65

Figure 1 shows the position of the centers of mass of the transmitter A at time t_A , the receiver B at time t_B , and the target object P at time t_O . The conceptual differences between these three times are particularly important. For instance, the position and velocity of the receiver B may change significantly between the time the radio signal is transmitted (t_A) and the time it is received (t_B). In calculations of the Doppler shift in the radio signal transmitted at time t_A , the state of the receiver B at time t_A is irrelevant; its state at time t_B is what matters. Here we first assume that t_A , t_B , and t_O are known somehow. Section 3.7 outlines how to determine t_A and t_O given t_B .

Errors in time definitions can hence have significant impact on the results of a radio occultation. Every quantity that will be defined in Section 3, whether a position, velocity, angle, or frequency, is associated with a particular time. In some cases, such as the positions of objects, the associated time is fairly obvious, but in other cases, such as distances between objects or angles between vectors, the associated time might be less obvious.

The coordinate frame shown in Figure 1 is defined as follows. The origin is at $\underline{x}_P(t_O)$. The unit vectors $\hat{r}(t_O)$, $\hat{z}(t_O)$, and $\hat{n}(t_O)$ satisfy:

$$\begin{aligned} \hat{z}(t_O) &= \frac{(\underline{x}_P(t_O) - \underline{x}_B(t_B))}{|(\underline{x}_P(t_O) - \underline{x}_B(t_B))|} \\ \hat{n}(t_O) &= \frac{(\underline{x}_A(t_A) - \underline{x}_P(t_O))}{|(\underline{x}_A(t_A) - \underline{x}_P(t_O))|} \times \hat{z} \\ \hat{r}(t_O) &= \hat{z} \times \hat{n} \end{aligned} \tag{2}$$

The unit vector $\hat{n}(t_O)$, which is not shown on Figure 1, points upwards out of the page. The definition of $\hat{z}(t_O)$ ensures that the r -component of $\underline{x}_B(t_B)$ is zero and the z -component of $\underline{x}_B(t_B)$ is negative, while the definition of $\hat{r}(t_O)$ ensures that the r -component of $\underline{x}_A(t_A)$ is positive. Assuming that this

frame is used when an occultation occurs, the z -component of $\underline{x}_A(t_A)$ must be positive as well. Many other possible coordinate frames exist; the rationale for emphasizing this particular coordinate frame is provided in Section 3.4.

3.2 Doppler shift — Effects of special and general relativity

According to equation 5.2.4 of Soffel (1989) and equation 7 of Häusler et al. (2007), the relationship between a transmitted frequency f_A and a received frequency f_B is:

$$\frac{f_B(t_B)}{f_A(t_A)} = \frac{1 - \frac{\underline{v}_B(t_B) \cdot \hat{\underline{n}}_B(t_B)}{c} - \frac{U_B(t_B)}{c^2} + \frac{v_B(t_B)^2}{2c^2}}{1 - \frac{\underline{v}_A(t_A) \cdot \hat{\underline{n}}_A(t_A)}{c} - \frac{U_A(t_A)}{c^2} + \frac{v_A(t_A)^2}{2c^2}} \quad (3)$$

Here \underline{v}_B is the velocity of the receiver, $\hat{\underline{n}}_B$ is the unit vector along which the radio wave propagates into the receiver, U_B is the gravitational potential at the receiver, \underline{v}_A is the velocity of the transmitter, $\hat{\underline{n}}_A$ is the unit vector along which the radio wave propagates away from the transmitter, and U_A is the gravitational potential at the transmitter. This expression is accurate to order $(v/c)^2$. Note that all the quantities in this equation ought to be referenced to the same inertial frame.

3.3 Introduction of the frequency residual

Suppose there is no refraction at the target object P . In this case, the radio signal travels directly from the transmitter to the receiver and the unit vectors $\hat{\underline{n}}_B(t_B)$ and $\hat{\underline{n}}_A(t_A)$ are equal. We label these as the “direct” unit vectors $\hat{\underline{n}}_{B,Direct}(t_B)$ and $\hat{\underline{n}}_{A,Direct}(t_A)$. The received radio frequency is $f_{B,Direct}(t_B)$.

1
2
3
4 If refraction of the radio signal occurs at the target object, as illustrated in
5
6 Figure 1, then these two unit vectors are different and we label these as the
7
8 “occultation” unit vectors $\hat{\underline{n}}_{B,Occ}(t_B)$ and $\hat{\underline{n}}_{A,Occ}(t_A)$. Now the received radio
9
10 frequency is $f_{B,Occ}(t_B)$.
11
12

13
14
15 The difference between $f_{B,Occ}(t_B)$ and $f_{B,Direct}(t_B)$ is known as the frequency
16
17 residual, $\Delta f(t_B)$. It can be found from the measured $f_{B,Occ}(t_B)$ and the theo-
18
19 retically calculated $f_{B,Direct}(t_B)$. It can also be related to the refractive prop-
20
21 erties of the target object.
22
23

$$\frac{\Delta f(t_B)}{f_A(t_A)} = \left(\frac{1 - \frac{\underline{v}_B(t_B) \cdot \hat{\underline{n}}_{B,Occ}(t_B)}{c} - \frac{U_B(t_B)}{c^2} + \frac{v_B(t_B)^2}{2c^2}}{1 - \frac{\underline{v}_A(t_A) \cdot \hat{\underline{n}}_{A,Occ}(t_A)}{c} - \frac{U_A(t_A)}{c^2} + \frac{v_A(t_A)^2}{2c^2}} \right) - \left(\frac{1 - \frac{\underline{v}_B(t_B) \cdot \hat{\underline{n}}_{B,Direct}(t_B)}{c} - \frac{U_B(t_B)}{c^2} + \frac{v_B(t_B)^2}{2c^2}}{1 - \frac{\underline{v}_A(t_A) \cdot \hat{\underline{n}}_{A,Direct}(t_A)}{c} - \frac{U_A(t_A)}{c^2} + \frac{v_A(t_A)^2}{2c^2}} \right) \quad (4)$$

24
25
26
27
28
29
30
31
32
33
34
35
36
37
38
39
40
41 Though the relativistic Equation 4 is used throughout this work for com-
42
43 pleteness, the Appendix describes the non-relativistic version of Equation 4.
44
45 The non-relativistic version provides an uncluttered perspective on the major
46
47 factors affecting the frequency residual, leading to the counter-intuitive result
48
49 that the frequency residual is dominated by the velocity component perpendic-
50
51 ular to, not parallel to, the line of sight. In the Mars Global Surveyor example
52
53 that will be introduced in Section 4, the ratios of the relativistic $(v/c)^2$ and
54
55 U/c^2 terms to the non-relativistic v/c term are both on the order of 1 part in
56
57 10^5 and relativistic effects are therefore insignificant. This is not always the
58
59 case.
60
61
62
63
64
65

3.4 Assumption of spherical symmetry

In order to proceed further with this expression, we must make a significant decision concerning the frame in which we shall work. In order for a particular radio ray to remain confined to the plane outlined in Figure 1, which greatly simplifies analysis, the refractive environment at the target object P must be spherically symmetric as encountered by the ray. That requires that our frame be moving with the target object P . Consequently, $\underline{v}_A(t_A)$ equals $\dot{\underline{x}}_A(t_A) - \dot{\underline{x}}_P(t_O)$, where an overdot indicates a derivative with respect to time, and $\underline{v}_B(t_B)$ equals $\dot{\underline{x}}_B(t_B) - \dot{\underline{x}}_P(t_O)$. We further define $vr_A(t_A)$ as the r -component of $\underline{v}_A(t_A)$, which equals $\underline{v}_A(t_A) \cdot \hat{\underline{r}}(t_O)$ and define $vz_A(t_A)$, $vr_B(t_B)$, and $vz_B(t_B)$ similarly.

The assumption of spherical symmetry introduces limitations that are addressed further in Section 5. One of the limitations is that our results will not apply to oblate planets, such as Jupiter, Saturn, Uranus, and Neptune. In such instances, gradients of refractivity exist perpendicular to the $r - z$ plane in Figure 1 that contains the transmitter, receiver, and target object and thus the radio signal will travel outside this plane (as required by Equation 1).

3.5 Angles

We next define four angles that are useful for describing the unit vectors in Equation 4: δ_B , β_A , δ_X , and β_X .

The angle δ_B is defined by:

$$\tan \delta_B = \frac{(r_A(t_A) - r_B(t_B))}{(z_A(t_A) - z_B(t_B))} \quad (5)$$

The angle β_A is defined by:

$$\beta_A + \delta_B = 90^\circ \quad (6)$$

Note that the definition of the coordinate system requires that $0^\circ < \delta_B < 90^\circ$ and $0^\circ < \beta_A < 90^\circ$ during an occultation. Hence $\cos \beta_A = \sin \delta_B$ and $\sin \beta_A = \cos \delta_B$.

The angle δ_X is defined by:

$$\tan(\delta_B - \delta_X) = \frac{(r_X(t_O) - r_B(t_B))}{(z_X(t_O) - z_B(t_B))} \quad (7)$$

The angle β_X is defined by:

$$\tan(\beta_A - \beta_X) = \frac{(r_A(t_A) - r_X(t_O))}{(z_A(t_A) - z_X(t_O))} \quad (8)$$

With these definitions, we have:

$$-\hat{\underline{n}}_{B,Direct}(t_B) = \hat{\underline{r}}(t_O) \sin \delta_B + \hat{\underline{z}}(t_O) \cos \delta_B \quad (9)$$

$$-\hat{\underline{n}}_{B,Occ}(t_B) = \hat{\underline{r}}(t_O) \sin(\delta_B - \delta_X) + \hat{\underline{z}}(t_O) \cos(\delta_B - \delta_X) \quad (10)$$

$$-\hat{\underline{n}}_{A,Direct}(t_A) = \hat{\underline{r}}(t_O) \cos \beta_A + \hat{\underline{z}}(t_O) \sin \beta_A \quad (11)$$

$$-\hat{\underline{n}}_{A,Occ}(t_A) = \hat{\underline{r}}(t_O) \cos(\beta_A - \beta_X) + \hat{\underline{z}}(t_O) \sin(\beta_A - \beta_X) \quad (12)$$

1
2
3
4 *3.6 Solution for unknown angles*
5
6
7
8

9 Thus, dropping the explicit time references for clarity, Equation 4 becomes:

10
11
12
13
14
15
16
17
18
19
20

$$\frac{\Delta f}{f_A} = \left(\frac{1 + \frac{vr_B \sin(\delta_B - \delta_X) + vz_B \cos(\delta_B - \delta_X)}{c} - \frac{U_B}{c^2} + \frac{v_B^2}{2c^2}}{1 + \frac{vr_A \cos(\beta_A - \beta_X) + vz_A \sin(\beta_A - \beta_X)}{c} - \frac{U_A}{c^2} + \frac{v_A^2}{2c^2}} \right) - \left(\frac{1 + \frac{vr_B \sin \delta_B + vz_B \cos \delta_B}{c} - \frac{U_B}{c^2} + \frac{v_B^2}{2c^2}}{1 + \frac{vr_A \cos \beta_A + vz_A \sin \beta_A}{c} - \frac{U_A}{c^2} + \frac{v_A^2}{2c^2}} \right) \quad (13)$$

21 With two exceptions, all the variables in Equation 13 are either known at
22 the appropriate times (Δf , f_A , c , U_A , U_B) or can be obtained from trajec-
23 tory information for the receiver A , transmitter B , and target object P (the
24 remaining variables). The two exceptions are the angles β_X and δ_X .
25
26
27
28
29

30 Thankfully, the two angles β_X and δ_X can also be related to the geometry
31 of the occultation. Since the spatial distribution of refractivity around the
32 target object P is spherically symmetric, then the closest approaches of the
33 two asymptotes to the center of mass of the target object P are identical.
34 This follows from the requirement that the ray path be invariant under time
35 reversal. We label this closest approach distance as the impact parameter, a ,
36 which satisfies the following two equations.
37
38
39
40
41
42
43
44
45

46
47
48
49

$$a(t_O) = -z_B(t_B) \sin(\delta_B - \delta_X) \quad (14)$$

50
51
52
53
54
55

$$a(t_O) = \left(r_A^2(t_A) + z_A^2(t_A) \right)^{1/2} \sin(\beta_A - \beta_X - \gamma) \quad (15)$$

56 where γ satisfies:

57
58
59
60
61
62
63
64
65

$$\tan \gamma = \frac{z_A(t_A)}{r_A(t_A)} \quad (16)$$

Note that the impact parameter, $a(t_O)$, does not equal $|\underline{x}_P(t_O) - \underline{x}_X(t_O)|$, as can be seen in Figure 1 and Fjeldbo et al. (1971). If the impact parameter $a(t_O)$ is eliminated from Equations 14–15, then we have:

$$-z_B(t_B) \sin(\delta_B - \delta_X) = \left(r_A^2(t_A) + z_A^2(t_A)\right)^{1/2} \sin(\beta_A - \beta_X - \gamma) \quad (17)$$

Again, with the exception of the angles β_X and δ_X , all the variables in Equation 17 can be obtained from trajectory information for the receiver A , transmitter B , and target object P . We have two equations (Equations 13 and 17) and two unknowns (β_X and δ_X). These two equations can be solved for the two unknowns, providing the values of β_X and δ_X for an individual radio ray. Note that a useful numerical technique for solving the non-relativistic versions of these two equations for the angles β_X and δ_X was introduced by Fjeldbo et al. (1971). After solutions for β_X and δ_X are obtained for all rays recorded at the receiver, the values of β_X and δ_X are known as functions of time during the occultation. From these, the total angle of refraction, α , and the impact parameter, a , can be obtained as functions of time.

$$\alpha = \beta_X + \delta_X \quad (18)$$

$$a(t_O) = \left(r_A^2(t_A) + z_A^2(t_A)\right)^{1/2} \sin(\beta_A - \beta_X - \gamma) \quad (19)$$

That achieves the objective of this Section, which was to obtain a series of bending angles as a function of impact parameter, from which neutral and plasma densities can then be determined.

3.7 Determination of times

In order for the technique outlined in Section 3 to be implemented, the times t_A , t_O , and t_B must be known. In principle, they and all quantities in Equation 4 should be referenced to the same inertial frame. That is, UTC times at the transmitter A , receiver B , and the target object P should be corrected for relativistic effects. We neglect that step in this analysis, since the results of an example based on Mars Global Surveyor data are acceptable without it.

Since we assume the existence of a time series of frequency residuals, the time of receipt, t_B , must be known. Since the transmitter A and the receiver B are both solar system objects, whether natural or artificial, following deterministic trajectories, the time of transmission, t_A , can be found from $|\underline{x}_A(t_A) - \underline{x}_B(t_B)| = c(t_B - t_A)$. Existing tools in SPICE can perform this calculation straightforwardly. However, the occultation point, \underline{x}_O , does not obey Newton's laws of motion and its trajectory is not known a priori. Accordingly, an iterative approach can be used to find t_O . The following assumes that the target object P is closer to the transmitter A than to the receiver B . Extension to the alternative case is trivial. Assume first that t_O equals the known t_A . Construct the direct, unrefracted ray path from the transmitter A at time t_A to the receiver B at time t_B and find the point along this line at which the separation between the line and the position of the target object P at time t_0 is minimum. Call this point the "pseudo-occultation point" and find the travel time Δt between the "pseudo-occultation point" and the position of transmitter A at t_A . The sum $t_A + \Delta t$ can be used as the new value of t_O and this iterative process can be repeated until acceptable convergence is achieved. Once the entire occultation data set has been processed and the actual set of

1
2
3
4 ray paths determined, then it can be verified that each “pseudo-occultation
5
6 point” is sufficiently close to its corresponding true occultation point for the
7
8 inferred set of occultation times t_0 to be deemed accurate.
9

10 11 12 13 **4 Demonstration using MGS data** 14

15 16 17 18 *4.1 Preamble* 19

20
21
22 The techniques developed in Section 3 were validated on a Mars Global Sur-
23
24 veyor (MGS) occultation at Mars. Here MGS is the transmitter, Earth the
25
26 receiver, and Mars the target object. Dave Hinson of the MGS radio science
27
28 team supplied us with time series of frequency residuals for an ingress occulta-
29
30 tion that occurred on 27 December 1998, during Phase 2 of MGS aerobraking
31
32 (Withers et al., 2003a), at a UTC time near 13:00. Their temporal resolution
33
34 is 0.4 seconds. The occultation geometry is shown in Figure 3.
35
36

37
38 We will compare our final results to the profiles of neutral atmospheric prop-
39
40 erties and ionospheric electron densities that were obtained by the MGS team
41
42 from this occultation and that have been archived at the Planetary Data Sys-
43
44 tem (PDS), where they bear the identifier 8361M48A. These archived profiles
45
46 were acquired from http://atmos.nmsu.edu/PDS/data/mors_1101/tps/1998_358/
47
48 and http://atmos.nmsu.edu/PDS/data/mors_1102/eds/1998_358/. The SPICE
49
50 kernels used were pck00009.tpc (rotational states of solar system objects),
51
52 de414.bsp (trajectories of solar system objects), naif0009.tls (record of leap
53
54 seconds), mgs_ab2.bsp (MGS trajectory), earthstns_fx_050714.bsp, and earth_topo_050714.tf,
55
56 and earth_720101_070426.bpc (trajectories of Deep Space network stations).
57
58 All these kernels were acquired from <http://naif.jpl.nasa.gov>.
59
60
61
62
63
64
65

4.2 *Time series of frequency residuals*

Several frequency residuals from the start and end of the file provided to us were discarded. Some residuals at early times (high altitudes) have unrealistically large values in comparison to adjacent ones, which are probably transient features associated with the start of the experiment. Some residuals at late times (low altitudes) have very low signal power, indicating that here the radio signal was affected by diffraction near the planet’s surface. The 2063 frequency residuals that were not discarded by this preprocessing are shown in Figure 2. The largest positive value of the frequency residuals, 0.06 Hz, corresponds to the ionosphere and the largest negative value of -10 Hz corresponds to the near-surface neutral atmosphere. The early frequency residuals correspond to rays that pass far above the atmosphere and ionosphere of Mars. Their standard deviation, 0.04 mHz, indicates the total noise present in the end-to-end experiment.

4.3 *Time series of bending angles and impact parameters*

The resultant values of the bending angle, α , and impact parameter, a , are shown in Figures 4–6. At Mars, which has a thin atmosphere, bending is minimal and the impact parameter a is approximately equal to the distance of closest approach. For reference, note that the mean equatorial radius of Mars is 3396.2 km and, according to the PDS documentation for this occultation, the radial distance to the surface at the location of this occultation is 3376.9 km. Since there are so many different conventions that can be used to convert radial distances into altitudes, we report our results in terms of radial distance for

1
2
3
4 clarity. The largest positive value of the bending angle α , 1.3×10^{-6} radians,
5
6 corresponds to the ionosphere and the largest negative value of -2×10^{-4}
7
8 radians corresponds to the near-surface neutral atmosphere. The standard
9
10 deviation of the high altitude bending angles, 8×10^{-8} radians, indicates the
11
12 total noise present in the end-to-end experiment. Note that some authors
13
14 adopt an alternative convention for the sign of the bending angle and have
15
16 positive bending angles in the neutral atmosphere (e.g. Ahmad and Tyler,
17
18 1998; Hinson et al., 1999; Withers, 2010).
19
20
21
22

23 *4.4 Refractivity profile*

24
25
26
27
28 The dependence of the refractive index, μ , on radial distance, R , can be ob-
29
30 tained from the dependence of bending angle, α , on impact parameter, a , as
31
32 described in Fjeldbo et al. (1971) and Withers (2010). As previously stated,
33
34 the point of closest approach of the radio signal transmitted at time t_A to
35
36 the target object P is \underline{x}_O , the time at which this radio signal is at this posi-
37
38 tion is t_O , and the two asymptotes of this ray path intersect at position \underline{x}_X .
39
40 The closest approach distance is $|\underline{x}_O(t_O) - \underline{x}_P(t_O)|$, which we now label as
41
42 $R(t_O) = R_O$. As shown in Appendix C of Fjeldbo et al. (1971), the value of
43
44 μ at $R = R_O$ satisfies:
45
46
47

$$48 \quad \pi \ln \mu(R_O) = \int_{a=a_O}^{a=\infty} \ln \left\{ \frac{a}{a_O} + \left[\left(\frac{a}{a_O} \right)^2 - 1 \right]^{1/2} \right\} \frac{d\alpha}{da} da \quad (20)$$

49
50
51
52
53
54 where a_O is $a(t_O)$. The integral relationship in Equation 20 is an example
55
56 of an Abel transform. Note that the upper boundary of this integral occurs
57
58 at $a = \infty$, whereas the available data do not extend that far. Also, from
59
60 Bouguer's rule (Born and Wolf, 1959; Fjeldbo et al., 1971; Kursinski et al.,
61
62
63
64
65

2000), the value of R_O satisfies:

$$R_O = \frac{a_O}{\mu(R_O)} \quad (21)$$

The value of μ at $R = R_O$ can be found for any R_O using the derived values of α and a , thereby yielding the function $\mu(R)$.

Figure 7 shows how refractivity, $\nu = \mu - 1$, depends on radial distance, R . In this instance, the time resolution of 0.4 seconds in the frequency residuals is equivalent to an altitude resolution of 0.6–1.2 km. Refractivity is positive in the neutral atmosphere ($\mu > 1$) and negative in the ionosphere ($\mu < 1$). Also shown in Figure 7 are refractivities associated with the archived profiles. The refractivities are not archived at the PDS; instead, they were provided to us by Dave Hinson. Figures 8–9 illustrate the differences between the derived and archived refractivities. Above 3420 km, the difference has a mean value of 8.6×10^{-11} and a standard deviation of 4.4×10^{-10} . Below 3420 km, the refractivities differ by less than 0.5%. In the following discussion, we assume that the refractivity is entirely attributable to the neutral atmosphere at $R < 3450$ km and to the ionosphere at $R > 3460$ km (Withers, 2010). At high altitudes the neutral density is not sufficient to affect the refractivity appreciably and at low altitudes the plasma density is not sufficient to affect the refractivity appreciably.

4.5 Ionospheric and atmospheric properties

Vertical profiles of the neutral and plasma number densities follow directly from the refractive index, μ (Withers, 2010). The total refractivity of the

1
2
3
4 atmosphere, $\nu = \mu - 1$, is the sum of the refractivity of the ionosphere, ν_e ,
5
6 and the refractivity of the neutral atmosphere, ν_n (Eshleman, 1973).
7
8

$$9 \quad \nu = \nu_e + \nu_n \quad (22)$$

10
11
12 For typical radio occultation experiments in planetary ionospheres, μ_e satisfies:
13
14

$$15 \quad \mu_e - 1 = \nu_e = -\frac{N_e e^2}{8\pi^2 m_e \epsilon_0 f^2} \quad (23)$$

16
17 Thus $N_e(r)$ can be determined from $\nu_e(r)$. Note that refractivity of the iono-
18
19 sphere is frequency-dependent.
20
21

22 The refractive index of the neutral atmosphere, μ_n , satisfies:
23
24
25

$$26 \quad \mu_n - 1 = \nu_n = \sum \kappa_i n_{n,i} \quad (24)$$

27
28 where κ_i is the refractive volume of constituent i and $n_{n,i}$ is the number density
29
30 of constituent i (Eshleman, 1973). The contributions of aerosols and conden-
31
32 sates, such as dust or clouds, to the refractivity of the neutral atmosphere
33
34 can be ignored because they do not affect the propagation of electromagnetic
35
36 waves at typical radio occultation frequencies. A mean refractive volume, κ ,
37
38 can be defined based on the known chemical composition of the atmosphere
39
40 such that:
41
42
43
44
45
46
47
48
49

$$50 \quad \nu_n = \kappa n_n \quad (25)$$

51
52 where n_n is the total neutral number density. Hence $n_n(r)$ can be found
53
54 from $\nu_n(r)$. Note that refractivity of the neutral atmosphere is not frequency-
55
56 dependent.
57
58
59
60
61
62
63
64
65

1
2
3
4 Figure 10A shows the electron density profile, which was obtained from the
5 refractivity profile using an assumed radio frequency of 8.423 GHz (Hinson
6 et al., 1999; Withers, 2010). Figure 10B illustrates the differences between
7 the derived and archived electron density profiles. The mean and standard
8 deviation of the differences are $2 \times 10^8 \text{ m}^{-3}$ and $7 \times 10^8 \text{ m}^{-3}$, respectively. The
9 average of the uncertainties in the archived electron density values is 1.9×10^9
10 m^{-3} , which indicates that the differences between the derived and archived
11 electron density profiles are not statistically significant.
12
13
14
15
16
17
18
19
20
21

22 Figure 11A shows the neutral number density profile, $n_n(R)$, which was ob-
23 tained from the refractivity profile using $1.804 \times 10^{-29} \text{ m}^3$ for the refractive
24 volume of the atmosphere. We simply assume the same value of the refractive
25 volume as was used by the MGS team (Hinson et al., 1999). The inferred neu-
26 tral number density is dominated by the experimental noise above 3440 km, so
27 the profiles of neutral atmospheric properties are truncated at 3440 km. Even
28 so, our derived neutral number densities extend to higher altitudes than the
29 archived values, presumably reflecting conservative choices by the MGS radio
30 science team regarding archiving policies. Figure 11B illustrates the differences
31 between the derived and archived neutral number density profiles. The derived
32 number densities are systematically larger than the archived number densities
33 by up to 0.4%, and the difference diminishes as altitude increases. These dif-
34 ferences could arise from choices regarding numerical integration techniques.
35
36
37
38
39
40
41
42
43
44
45
46
47
48
49
50
51
52
53
54
55
56
57
58
59
60
61
62
63
64
65

The mass density profile, $\rho(R)$, can be found from $n_n(R)$ and the atmospheric
mean molecular mass, which was stated to be $7.221 \times 10^{-26} \text{ kg}$, independent

1
2
3
4 of altitude, by Hinson et al. (1999). The mass density profile is shown in
5
6 Figure 11C. Since the archived neutral atmospheric properties do not include
7
8 mass densities, we calculated an “archived” mass density profile using our
9
10 assumed mean molecular mass. This is shown in Figure 11C as a reference.
11
12 Figure 11D, which compares the two mass density profiles, is included for
13
14 consistency, although our assumptions make it identical to Figure 11B.
15
16
17
18

19 The pressure profile, $p(R)$, can be found from $\rho(R)$, the known gravitational
20
21 field, and an upper boundary condition via the equation of hydrostatic equi-
22
23 librium. Multiple models exist for the gravitational field of Mars, which varies
24
25 with latitude and longitude. In order to ensure that our assumptions were con-
26
27 sistent with those of the MGS team, we inferred the gravitational acceleration,
28
29 g , actually used by the MGS team from $g = -dp/dz \times 1/\rho$ via the archived
30
31 densities and pressure gradients. The result was consistent with $g = GM/R^2$,
32
33 where $GM = 4.26 \times 10^{13} \text{ m}^3 \text{ s}^{-2}$. The upper boundary condition can be an as-
34
35 sumed temperature or pressure. It can also be obtained from the scale height of
36
37 $n_n(R)$ under certain reasonable assumptions (Withers et al., 2003b; Tellmann
38
39 et al., 2009). Here we find the scale height, H , for neutral number densities
40
41 between 3430 km and 3440 km, which equals 6.2 km, and assume $p(3440 \text{ km})$
42
43 $= \rho(3440 \text{ km}) \times g(3440 \text{ km}) \times H$. Errors in the upper boundary condition
44
45 have minimal effect on the derived pressures at altitudes more than several
46
47 scale heights below the upper boundary (Withers et al., 2003b). Figure 11E
48
49 shows the neutral pressure profile and Figure 11F illustrates the differences
50
51 between the derived and archived neutral pressure profiles. As with the neu-
52
53 tral number densities and for the same reason, our derived pressures extend
54
55 to higher altitudes than the archived values. The large differences between
56
57 derived and archived pressures at high altitudes is hence simply the outcome
58
59
60
61
62
63
64
65

1
2
3
4 of slight inconsistencies in upper boundary conditions, which is most visible
5
6 as the offset in temperatures at the top of the archived profile. The effects of
7
8 imposed upper boundary conditions diminish as altitude decreases and the dif-
9
10 ference between derived and archived pressures levels off at 0.3%–0.4%, which
11
12 is consistent with the differences in neutral number density in Figure 11B.
13
14 The effects of the upper boundary condition are illustrated by an alternate
15
16 neutral pressure profile that was obtained using a different upper condition,
17
18 one chosen to improve agreement with the PDS profile. This alternate profile
19
20 is shown by the dotted lines in Figures 11E and F. The difference between al-
21
22 ternate and archived pressures is everywhere less than 0.4%, again consistent
23
24 with the differences in neutral number density in Figure 11B.
25
26
27
28
29

30 The temperature profile, $T(R)$, can be found from $p(R)$, the atmospheric com-
31
32 position and either $n_n(R)$ or $\rho(R)$ via an equation of state, such as the ideal
33
34 gas law. Errors in the upper boundary condition of the equation of hydrostatic
35
36 equilibrium have minimal effect on the derived temperatures at altitudes more
37
38 than several scale heights below the upper boundary (Withers et al., 2003b).
39
40 Here we used the ideal gas law with our assumed mean molecular mass. Fig-
41
42 ure 11G shows the neutral temperature profile and Figure 11H illustrates
43
44 the differences between the derived and archived neutral temperature profiles.
45
46 Differences are noticeable at high altitudes due to slight inconsistencies in
47
48 assumed upper boundary conditions, but are less than 0.1 K at the lowest
49
50 altitudes. The effects of the upper boundary condition are illustrated by an
51
52 alternate neutral temperature profile that was obtained using the alternate
53
54 neutral pressure profile shown in Figure 11E. This alternate profile is shown
55
56 by the dotted lines in Figures 11G and H. The difference between alternate and
57
58 archived temperatures is everywhere less than 0.5 K and the mean difference
59
60
61
62
63
64
65

1
2
3
4 is 0.1 K.
5
6
7
8

9 **5 Limitations**

10
11
12
13
14 There are many types of radio occultation experiments and the methods pro-
15
16 vided here do not apply to all of them. Our methods assume a (1) one-way (2)
17
18 single frequency experiment with a transmitter that has a (3) stable frequency
19
20 source and a target object whose atmosphere and ionosphere can be assumed
21
22 to be (4) spherically symmetric, for which (5) frequency residuals have al-
23
24 ready been obtained from raw data. Each numbered point is responsible for
25
26 limitations in our methods, as enumerated below.
27
28
29

30 (1) In two-way experiments such as those performed by Mars Express, the ra-
31
32 dio signal propagates through the atmosphere/ionosphere twice, with the ray
33
34 passing through different regions on the uplink and downlink legs (Pätzold
35
36 et al., 2004). Separation of the refraction experienced in the neutral atmo-
37
38 sphere on the two legs is challenging and beyond the scope of the current work.
39
40 However, the refraction experienced in the ionosphere, which is frequency-
41
42 dependent, is readily separated (Pätzold et al., 2004). (2) In multi-frequency
43
44 experiments such as those performed by Cassini, comparison of frequency
45
46 residuals at different frequencies can isolate ionospheric refraction and elimi-
47
48 nate many sources of error (Kliore et al., 2004; Pätzold et al., 2004; Häusler
49
50 et al., 2006). Of course, a multi-frequency downlink experiment can also be
51
52 considered as a set of independent single frequency downlink experiments.
53
54 (3) If the spacecraft does not have a stable frequency source, such as an ul-
55
56 trastable oscillator, then acceptable measurement accuracy requires that the
57
58 spacecraft merely serve as a transponder for a signal transmitted and received
59
60
61
62
63
64
65

1
2
3
4 elsewhere, most likely at a ground station equipped with a stable frequency
5 source (Pätzold et al., 2004). Consequently, the occultation must be a two-
6 way occultation. (4) If the atmosphere and ionosphere of the target object
7 cannot be assumed to be spherically symmetric, then gradients of refractiv-
8 ity will exist perpendicular to the $r - z$ plane in Figure 1 that contains the
9 transmitter, receiver, and target object, and thus the radio signal will travel
10 outside this plane (see Equation 1). Our methods will not perform well at the
11 oblate giant planets (Kliore et al., 1974, 1975; Hubbard et al., 1975; Lindal,
12 1992). However, many atmospheres and ionospheres in the solar system can
13 be assumed to be spherically symmetric, including those of the Sun, Mercury,
14 Venus, Earth, the Moon, Mars, the four Galilean satellites, Titan, Enceladus,
15 and Triton. (5) This work does not address how to produce frequency residu-
16 als from raw data, so is only immediately applicable in cases where frequency
17 residuals are archived. Frequency residuals from Venus Express and Mars Ex-
18 press are known to be available at archives, though the methods developed in
19 this work are not able to tackle the two-way occultations of Mars Express, and
20 it is possible that frequency residuals from other missions exist in archives we
21 have yet to discover. Although Equation 3 is central to finding the predicted
22 “direct” received frequency, there are a great many additional subtleties that
23 must be considered and we intend to address this topic in future work.

24
25
26
27
28
29
30
31
32
33
34
35
36
37
38
39
40
41
42
43
44
45
46
47
48
49
50 Readers considering using the methods outlined in this work should also bear
51 in mind that: A. Even archived frequency residuals may contain offsets or
52 drifts due to incomplete knowledge of either the spacecraft trajectory or other
53 contributions to the Doppler shift, which will particularly impact results in the
54 relatively unrefractive ionosphere (elimination of these potential ionospheric
55 problems in a multi-frequency occultation is one major factor that favors this

1
2
3
4 type of experiment). B. Noise and other effects can cause the bending angle
5 and impact parameter not to be monotonic functions of time, yet the Abel
6 transform from bending angle and impact parameter to refractivity and ra-
7 dial distance requires the series of impact parameters to vary monotonically.
8
9 C. Diffraction effects near the surfaces of solid target objects and multipath
10 propagation effects can lead to erroneous results if they are not corrected
11 for. Back-propagation analysis methods exist that can handle diffraction and
12 multipath effects (Karayel and Hinson, 1997; Marouf et al., 1986). As these
13 methods go beyond the limitations of ray-based geometrical optics, they per-
14 mit sub-Fresnel scale spatial resolution.
15
16
17
18
19
20
21
22
23
24
25
26

27 Despite the limitations of the methods described here, and despite the fact
28 that the state-of-the-art tools used by radio science teams at JPL, Stanford,
29 and Cologne are unquestionably more sophisticated than those described in
30 this work, this work still has value. Specifically, this work makes a functional
31 tool for investigating and analyzing radio occultation data available to all.
32
33
34
35
36
37
38
39
40

41 **6 Discussion and conclusions**

42
43
44

45 Raw radio occultation data are hard to process into scientifically useful data
46 products and the necessary skills are not widespread. Here we have provided
47 detailed instructions and accompanying software for one critical aspect of ra-
48 dio occultation data processing: how to obtain a series of bending angles α as a
49 function of the ray impact parameter a from a time series of frequency residu-
50 als. The software also performs the next step of converting bending angles and
51 impact parameters into vertical profiles of ionospheric electron density, neu-
52 tral atmospheric number density, mass density, pressure, and temperature, all
53
54
55
56
57
58
59
60
61
62
63
64
65

1
2
3
4 quantities that are scientifically useful. It is critically important to work in
5
6 a frame centered on and moving with the target object, since only in that
7
8 frame does a radio ray encounter a spherically symmetric atmosphere, and to
9
10 account for light travel times throughout the analysis.
11
12

13
14 However, these specific methods are limited. As currently developed, they are
15
16 valid only for a one-way, single frequency, downlink experiment with a trans-
17
18 mitter that has a stable frequency source and a target object whose atmosphere
19
20 and ionosphere can be assumed to be spherically symmetric. These methods
21
22 cannot be immediately applied to two-way radio occultations, such as Mars
23
24 Express, in which a radio signal propagates twice through the atmosphere
25
26 and ionosphere of the target object or to giant planet occultations, where
27
28 the atmosphere and ionosphere of the target object are significantly oblate.
29
30 They also require that raw radio occultation data have been pre-processed
31
32 to the frequency residuals stage. Yet they provide the wider community with
33
34 some much-needed abilities to work with radio occultation data and they are
35
36 a necessary foundation for anticipated development into a more general tool.
37
38
39
40

41 These methods were demonstrated successfully on data from a Mars Global
42
43 Surveyor occultation at Mars. The differences between the derived and archived
44
45 electron densities are only about one-third of the uncertainty in the archived
46
47 electron densities, a difference which is equivalent to less than 0.5% of the sub-
48
49 solar peak electron density. If the upper boundary condition imposed for the
50
51 equation of hydrostatic equilibrium is guided by the archived neutral profiles,
52
53 then derived and archived neutral profiles differ by less than 0.4% (densities
54
55 and pressures) or 0.5 K (temperatures). These results are close enough to
56
57 demonstrate that our processing programs are working well. The remaining
58
59 improvements that are required are likely incremental, rather than substan-
60
61
62
63
64
65

1
2
3
4
5
6
7
8
9
10
11
12
13
14
15
16
17
18
19
20
21
22
23
24
25
26
27
28
29
30
31
32
33
34
35
36
37
38
39
40
41
42
43
44
45
46
47
48
49
50
51
52
53
54
55
56
57
58
59
60
61
62
63
64
65

tial. These differences may be caused by differences in the implementation of the Abel transform used to derive refractive index or in the generic SPICE kernels. The uncertainties in our results have not been quantified yet. The uncertainty in the frequency residuals, 0.04 mHz, is readily calculated, but the propagation of these uncertainties through the Abel transform and other processing steps is sufficiently non-trivial to merit careful attention in a separate manuscript (e.g., Lipa and Tyler, 1979).

Computer programs that implement the data processing methods outlined here using the IDL programming language accompany this manuscript. We encourage readers to inspect them and run them using the examples provided and other recordings of time series of frequency residuals. The tools provided here are sufficiently powerful that readers can recreate atmospheric and ionospheric profiles for old missions whose final profiles are not widely available. We also hope that readers will improve these programs and make their improvements publicly available. This will enhance the quality of any recreated atmospheric and ionospheric profiles and further improve the radio occultation data processing skills of the broad planetary science community.

Appendix: Non-relativistic frequency residual

If relativistic terms of order U/c^2 or $(v/c)^2$ and higher can be neglected, then Equation 4 becomes:

$$\frac{\Delta f(t_B)}{f_A(t_A)} = \frac{v_A(t_A)}{c} \cdot (\hat{n}_{A,Occ}(t_A) - \hat{n}_{A,Direct}(t_A)) - \frac{v_B(t_B)}{c} \cdot (\hat{n}_{B,Occ}(t_B) - \hat{n}_{B,Direct}(t_B)) \quad (26)$$

1
2
3
4 This emphasizes that the root causes of the frequency residual are the differ-
5
6
7
8
9
10
11
12
13
14
15
16
17
18
19
20
21
22
23
24
25
26
27
28
29
30
31
32
33
34
35
36
37
38
39
40
41
42
43
44
45
46
47
48
49
50
51
52
53
54
55
56
57
58
59
60
61
62
63
64
65

This emphasizes that the root causes of the frequency residual are the differences in ray propagation directions at the transmitter and receiver. For the MGS-like case in which the target object P is much closer to the transmitter A than to the receiver B , $\delta_X \ll \beta_X$ and $|\hat{\underline{n}}_{B,Occ}(t_B) - \hat{\underline{n}}_{B,Direct}(t_B)| \ll |\hat{\underline{n}}_{A,Occ}(t_A) - \hat{\underline{n}}_{A,Direct}(t_A)|$.

Hence Equation 26 is approximately:

$$\frac{\Delta f(t_B)}{f_A(t_A)} = \frac{\underline{v}_A(t_A)}{c} \cdot (\hat{\underline{n}}_{A,Occ}(t_A) - \hat{\underline{n}}_{A,Direct}(t_A)) \quad (27)$$

Since $\delta_X \ll \beta_X$ means that $\beta_X = \alpha$, we can write $\hat{\underline{n}}_{A,Occ}(t_A)$ in terms of $\hat{\underline{n}}_{A,Direct}(t_A)$ and α :

$$\hat{\underline{n}}_{A,Occ}(t_A) = \hat{\underline{n}}_{A,Direct}(t_A) \cos \alpha + (\hat{\underline{n}}_{A,Direct}(t_A) \times \hat{\underline{n}}(t_O)) \sin \alpha \quad (28)$$

where $\hat{\underline{n}}(t_O)$ is one of the unit vectors defining our frame (Equation 2). Substituting this into Equation 27 leads to:

$$\frac{\Delta f(t_B)}{f_A(t_A)} = \frac{\underline{v}_A(t_A)}{c} \cdot (\hat{\underline{n}}_{A,Direct}(t_A) (\cos \alpha - 1) + (\hat{\underline{n}}_{A,Direct}(t_A) \times \hat{\underline{n}}(t_O)) \sin \alpha) \quad (29)$$

For small bending angles, as long as $\underline{v}_A(t_A)$ is not nearly parallel with $\hat{\underline{n}}_{A,Direct}(t_A)$, this reduces to:

$$\frac{\Delta f(t_B)}{f_A(t_A)} = \frac{\underline{v}_A(t_A)}{c} \cdot (\hat{\underline{n}}_{A,Direct}(t_A) \times \hat{\underline{n}}(t_O)) \alpha \quad (30)$$

That is, $\Delta f = v_{\perp} \alpha / \lambda$, where v_{\perp} is the component of the transmitter's velocity relative to the target object that is in the transmitter-target object-receiver plane and perpendicular to the line of sight between the transmitter A and

1
2
3
4
5
6
7
8
9
10
11
12
13
14
15
16
17
18
19
20
21
22
23
24
25
26
27
28
29
30
31
32
33
34
35
36
37
38
39
40
41
42
43
44
45
46
47
48
49
50
51
52
53
54
55
56
57
58
59
60
61
62
63
64
65

the receiver B . It is counter-intuitive that a difference in frequency connected with a Doppler shift is controlled by the velocity component perpendicular to, not parallel to, the line of sight.

Acknowledgements

We thank the Mars Express and Venus Express radio science teams for helpful discussions and Dave Hinson for MGS data products and extremely valuable comments. This manuscript was immeasurably improved by comments from Mike Bird, Silvia Tellmann, and an anonymous reviewer.

References

- Ahmad, B., Tyler, G. L., 1998. The two-dimensional resolution kernel associated with retrieval of ionospheric and atmospheric refractivity profiles by Abelian inversion of radio occultation phase data. *Radio Sci.* 33, 129–142.
- Anthes, R. A., Bernhardt, P. A., Chen, Y., Cucurull, L., Dymond, K. F., Ector, D., Healy, S. B., Ho, S.-P., Hunt, D. C., Kuo, Y.-H., Liu, H., Manning, K., McCormick, C., Meehan, T. K., Randel, W. J., Rocken, C., Schreiner, W. S., Sokolovskiy, S. V., Syndergaard, S., Thompson, D. C., Trenberth, K. E., Wee, T.-K., Yen, N. L., Zeng, Z., 2008. The COSMIC/FORMOSAT-3 mission: Early results. *Bull. Am. Met. Soc.* 89, 313–333.
- Born, M., Wolf, E., 1959. *Principles of optics*. Pergamon Press, London.
- Eshleman, V. R., 1973. The radio occultation method for the study of planetary atmospheres. *Planet. Space Sci.* 21, 1521–1531.
- Fjeldbo, G., Kliore, A. J., Eshleman, V. R., 1971. The neutral atmosphere of Venus as studied with the Mariner V radio occultation experiments. *Astron. J.* 76, 123–140.
- Häusler, B., Pätzold, M., Tyler, G. L., Barriot, J., Bird, M. K., Dehant, V., Hinson, D., Simpson, R. A., Treumann, R. A., Eidel, W., Mattei, R., Rosenblatt, P., Remus, S., Selle, J., 2007. Venus atmospheric, ionospheric, surface and interplanetary radio-wave propagation studies with the VeRA Radio-Science Experiment. ESA SP-1295: Venus Express, available online at <http://sci.esa.int/venus-express/41535-vera-radio-science-experiment/>, pp. 1–30.
- Häusler, B., Pätzold, M., Tyler, G. L., Simpson, R. A., Bird, M. K., Dehant, V., Barriot, J., Eidel, W., Mattei, R., Remus, S., Selle, J., Tellmann, S., Imamura, T., 2006. Radio science investigations by VeRa onboard the Venus

- 1
2
3
4 Express spacecraft. *Planet. Space Sci.* 54, 1315–1335.
5
6 Hinson, D. P., Simpson, R. A., Twicken, J. D., Tyler, G. L., Flasar, F. M.,
7
8 1999. Initial results from radio occultation measurements with Mars Global
9
10 Surveyor. *J. Geophys. Res.* 104, 26997–27012.
11
12 Hu, X., Wu, X.-C., Gong, X.-Y., Wang, X., Xu, Q.-C., Jan. 2010. An Emula-
13
14 tion Research on the Radio Occultation Exploration of Martian Ionosphere.
15
16 *Chinese Astron. Astrophys.* 34, 100–112.
17
18 Hubbard, W. B., Hunten, D. M., Kliore, A., 1975. Effect of the Jovian oblate-
19
20 ness on Pioneer 10/11 radio occultations. *Geophys. Res. Lett.* 2, 265–268.
21
22 Imamura, T., Nabatov, A., Mochizuki, N., Iwata, T., Hanada, H., Matsumoto,
23
24 K., Noda, H., Kono, Y., Liu, Q., Futaana, Y., Ando, H., Yamamoto, Z.,
25
26 Oyama, K.-I., Saito, A., 2012. Radio occultation measurement of the elec-
27
28 tron density near the lunar surface using a subsatellite on the SELENE
29
30 mission. *J. Geophys. Res.* 117, A06303, 10.1029/2011JA017293.
31
32 Imamura, T., Toda, T., Tomiki, A., Hirahara, D., Hayashiyama, T.,
33
34 Mochizuki, N., Yamamoto, Z.-I., Abe, T., Iwata, T., Noda, H., Futaana,
35
36 Y., Ando, H., Häusler, B., Pätzold, M., Nabatov, A., 2011. Radio occulta-
37
38 tion experiment of the Venus atmosphere and ionosphere with the Venus
39
40 orbiter Akatsuki. *Earth, Planets, and Space* 63, 493–501.
41
42 Karayel, E. T., Hinson, D. P., 1997. Sub-Fresnel-scale vertical resolution in
43
44 atmospheric profiles from radio occultation. *Radio Sci.* 32, 411–424.
45
46 Kliore, A., Cain, D. L., Fjeldbo, G., Seidel, B. L., Rasool, S. I., 1974. Pre-
47
48 liminary results on the atmospheres of Io and Jupiter from the Pioneer 10
49
50 S-band occultation experiment. *Science* 183, 323–324.
51
52 Kliore, A., Cain, D. L., Levy, G. S., Eshleman, V. R., Fjeldbo, G., Drake,
53
54 F. D., 1965. Occultation experiment: Results of the first direct measurement
55
56 of Mars’s atmosphere and ionosphere. *Science* 149, 1243–1248.
57
58
59
60
61
62
63
64
65

- 1
2
3
4 Kliore, A., Fjeldbo, G., Seidel, B. L., Sesplaukis, T. T., Sweetnam, D. W.,
5
6 Woiceshyn, P. M., 1975. Atmosphere of Jupiter from the Pioneer 11 S-band
7
8 occultation experiment — Preliminary results. *Science* 188, 474–476.
9
- 10 Kliore, A. J., Anderson, J. D., Armstrong, J. W., Asmar, S. W., Hamilton,
11
12 C. L., Rappaport, N. J., Wahlquist, H. D., Ambrosini, R., Flasar, F. M.,
13
14 French, R. G., Iess, L., Marouf, E. A., Nagy, A. F., 2004. Cassini Radio
15
16 Science. *Space Sci. Rev.* 115, 1–70.
17
18
- 19 Kursinski, E. R., Hajj, G.-A., Leroy, S. S., Herman, B., 2000. The GPS radio
20
21 occultation technique. *Terr. Atmos. Oceanic Sci.* 11, 53–114.
22
23
- 24 Kursinski, E. R., Hajj, G. A., Schofield, J. T., Linfield, R. P., Hardy, K. R.,
25
26 1997. Observing Earth’s atmosphere with radio occultation measurements
27
28 using the Global Positioning System. *J. Geophys. Res.* 102, 23429–23465.
29
- 30 Lindal, G. F., 1992. The atmosphere of Neptune — An analysis of radio oc-
31
32 cultation data acquired with Voyager 2. *Astron. J.* 103, 967–982.
33
- 34 Lipa, B., Tyler, G. L., 1979. Statistical and computational uncertainties in
35
36 atmospheric profiles from radio occultation — Mariner 10 at Venus. *Icarus*
37
38 39, 192–208.
39
- 40 Marouf, E. A., Tyler, G. L., Rosen, P. A., 1986. Profiling Saturn’s rings by
41
42 radio occultation. *Icarus* 68, 120–166.
43
44
- 45 Nicholson, P. D., Muhleman, D. O., 1978. Independent radio-occultation stud-
46
47 ies of Venus’ atmospheres. *Icarus* 33, 89–101.
48
- 49 Noguchi, K., Imamura, T., Oyama, K.-I., Nabatov, A. S., 2002. Radio-
50
51 occultation projects in space programs of Japan. *Radio Sci. Bull.* 303, 27–31.
52
53
- 54 Oyama, K.-I., Nabatov, A. S., Savich, N. A., Yamamoto, Z., Imamura, T.,
55
56 Ichikawa, T., Noguchi, K., 2001. First test of the NOZOMI radio science
57
58 system in actual space flight. *Adv. Space Res.* 27, 1847–1850.
59
- 60 Pätzold, M., Häusler, B., Aksnes, K., Anderson, J. D., Asmar, S. W., Barriot,
61
62
63
64
65

- 1
2
3
4 J.-P., Bird, M. K., Boehnhardt, H., Eidel, W., Grün, E., Ip, W. H., Marouf,
5
6 E., Morley, T., Neubauer, F. M., Rickman, H., Thomas, N., Tsurutani,
7
8 B. T., Wallis, M. K., Wickramasinghe, N. C., Mysen, E., Olson, O., Remus,
9
10 S., Tellmann, S., Andert, T., Carone, L., Fels, M., Stanzel, C., Audenrieth-
11
12 Kersten, I., Gahr, A., Müller, A.-L., Stupar, D., Walter, C., 2007. Rosetta
13
14 Radio Science Investigations (RSI). *Space Sci. Rev.* 128, 599–627.
- 15
16
17 Pätzold, M., Neubauer, F. M., Carone, L., Hagermann, A., Stanzel, C.,
18
19 Häusler, B., Remus, S., Selle, J., Hagl, D., Hinson, D. P., Simpson,
20
21 R. A., Tyler, G. L., Asmar, S. W., Axford, W. I., Hagfors, T., Barriot,
22
23 J.-P., Cerisier, J.-C., Imamura, T., Oyama, K.-I., Janle, P., Kirchengast,
24
25 G., Dehant, V., 2004. MaRS: Mars Express Orbiter Radio Science.
26
27 ESA SP-1240: Mars Express: the Scientific Payload, available online at
28
29 <http://sci.esa.int/science-e/www/object/index.cfm?fobjectid=34885>, pp.
30
31 141–163.
- 32
33
34 Phinney, R. A., Anderson, D. L., 1968. On the radio occultation method for
35
36 studying planetary atmospheres. *J. Geophys. Res.* 73, 1819–1827.
- 37
38
39 Schinder, P. J., Flasar, F. M., Marouf, E. A., French, R. G., McGhee, C. A.,
40
41 Kliore, A. J., Rappaport, N. J., Barbini, E., Fleischman, D., Anabtawi,
42
43 A., 2011a. Saturn’s equatorial oscillation: Evidence of descending thermal
44
45 structure from Cassini radio occultations. *Geophys. Res. Lett.* 38, L08205,
46
47 10.1029/2011GL047191.
- 48
49
50 Schinder, P. J., Flasar, F. M., Marouf, E. A., French, R. G., McGhee, C. A.,
51
52 Kliore, A. J., Rappaport, N. J., Barbini, E., Fleischman, D., Anabtawi, A.,
53
54 2011b. The structure of Titan’s atmosphere from Cassini radio occultations.
55
56 *Icarus* 215, 460–474.
- 57
58
59 Schinder, P. J., Flasar, F. M., Marouf, E. A., French, R. G., McGhee, C. A.,
60
61 Kliore, A. J., Rappaport, N. J., Barbini, E., Fleischman, D., Anabtawi, A.,
62
63
64
65

- 1
2
3
4 2012. The structure of Titan’s atmosphere from Cassini radio occultations:
5
6 Occultations from the Prime and Equinox missions. *Icarus* 221, 1020–1031.
7
8
9 Soffel, M. H., 1989. *Relativity in Astrometry, Celestial Mechanics and*
10 *Geodesy*. Springer-Verlag, New York.
11
12
13 Tellmann, S., Pätzold, M., Häusler, B., Bird, M. K., Tyler, G. L., 2009.
14
15 Structure of the Venus neutral atmosphere as observed by the Radio Sci-
16
17 ence experiment VeRa on Venus Express. *J. Geophys. Res.* 114, E00B36,
18
19 10.1029/2008JE003204.
20
21 Withers, P., 2010. Prediction of uncertainties in atmospheric properties mea-
22 sured by radio occultation experiments. *Adv. Space Res.* 46, 58–73.
23
24 Withers, P., Bougher, S. W., Keating, G. M., 2003a. The effects of
25
26 topographically-controlled thermal tides in the martian upper atmosphere
27
28 as seen by the MGS accelerometer. *Icarus* 164, 14–32.
29
30
31 Withers, P., Towner, M. C., Hathi, B., Zarnecki, J. C., 2003b. Analysis of
32 entry accelerometer data: A case study of Mars Pathfinder. *Planet. Space*
33 *Sci.* 51, 541–561.
34
35
36
37
38
39 Yakovlev, O. I., 2002. *Space radio science*. Taylor and Francis, New York.
40
41
42
43
44
45
46
47
48
49
50
51
52
53
54
55
56
57
58
59
60
61
62
63
64
65

1
2
3
4
5
6
7
8
9
10
11
12
13
14
15
16
17
18
19
20
21
22
23
24
25
26
27
28
29
30
31
32
33
34
35
36
37
38
39
40
41
42
43
44
45
46
47
48
49
50
51
52
53
54
55
56
57
58
59
60
61
62
63
64
65

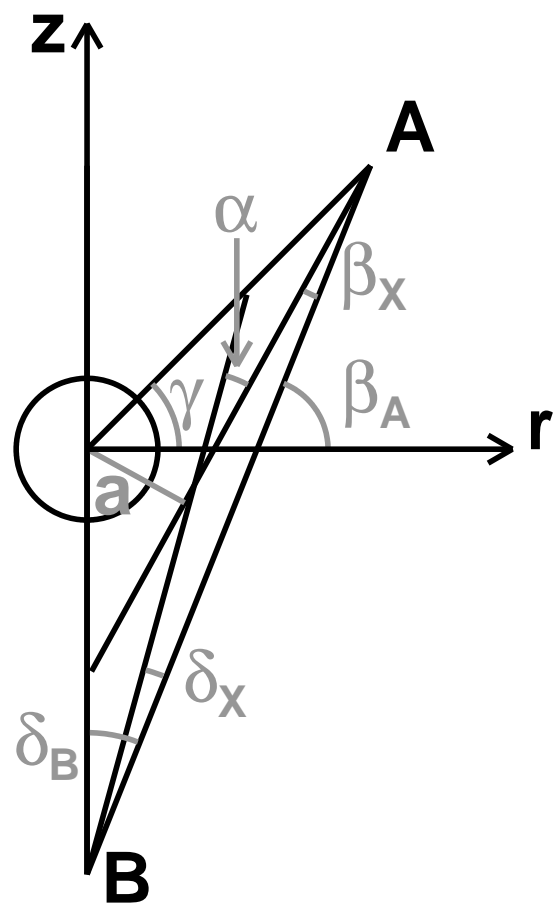


Fig. 1. Geometry for an occultation involving transmitter A , receiver B , and target object P at the origin. The remaining symbols are defined in the text. The position \underline{x}_X lies at the intersection of the two asymptotes to the ray path and the position \underline{x}_O lies close to \underline{x}_X .

1
2
3
4
5
6
7
8
9
10
11
12
13
14
15
16
17
18
19
20
21
22
23
24
25
26
27
28
29
30
31
32
33
34
35
36
37
38
39
40
41
42
43
44
45
46
47
48
49
50
51
52
53
54
55
56
57
58
59
60
61
62
63
64
65

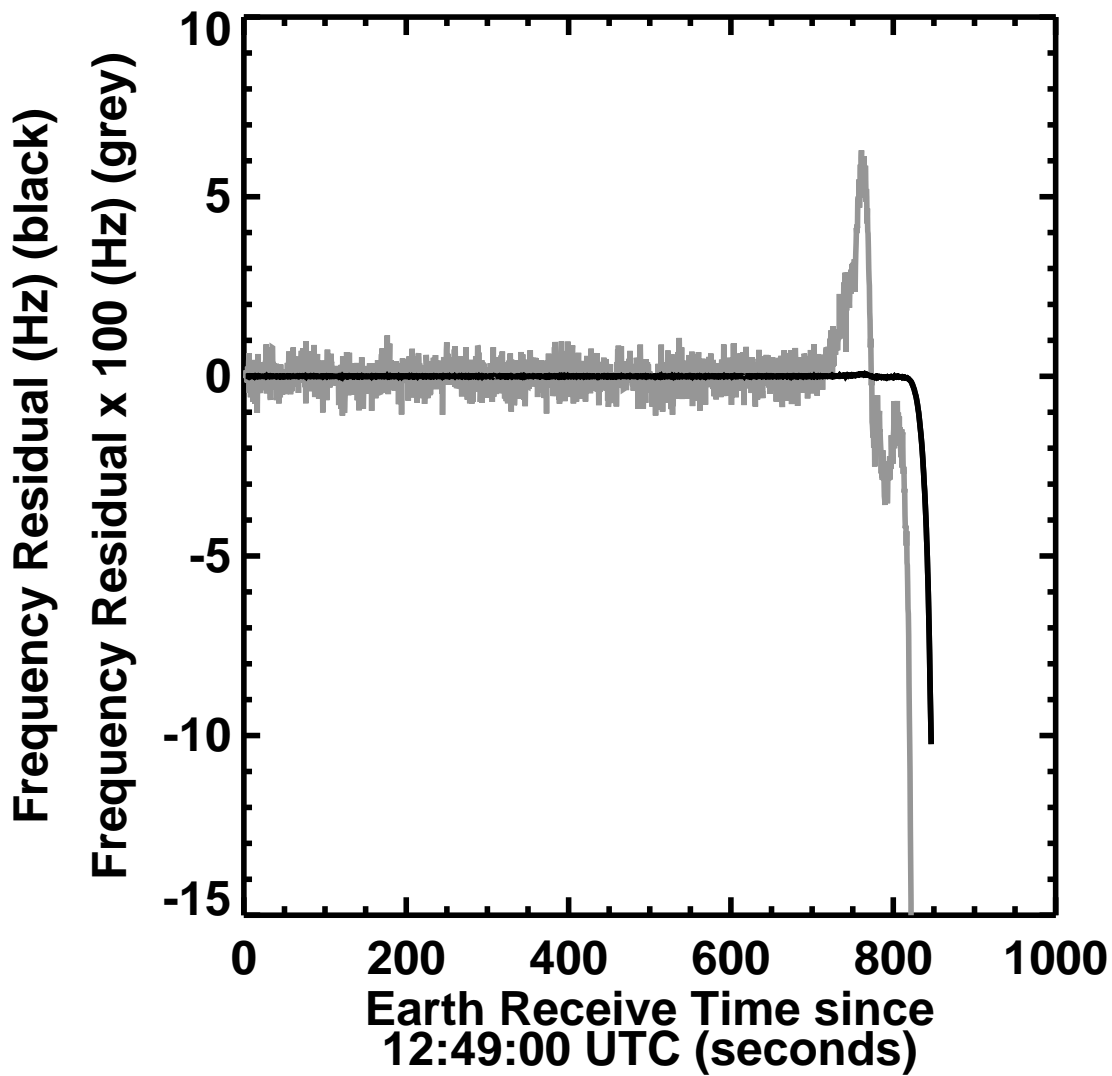


Fig. 2. Time series of frequency residuals for MGS occultation 8361M48A. The black line shows original frequency residuals and the grey line shows $100 \times$ the frequency residuals, which highlights the positive residuals caused by the ionosphere.

MGS Occultation Geometry

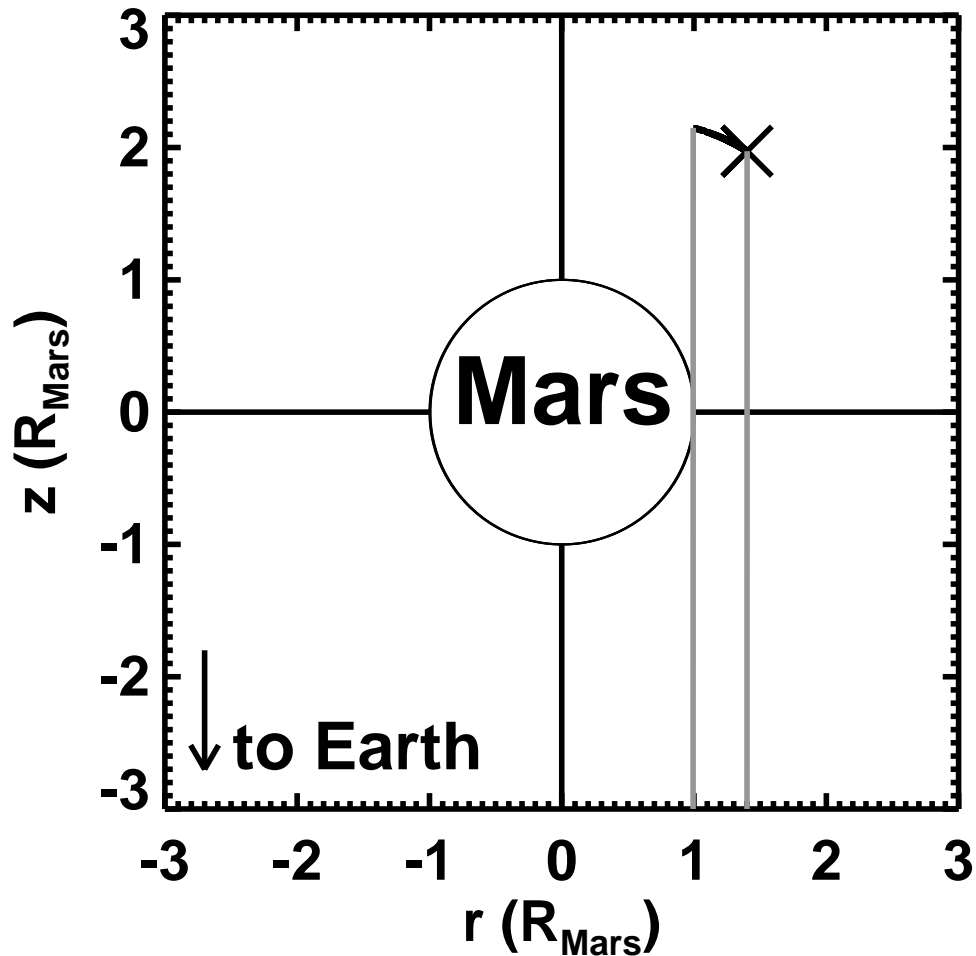


Fig. 3. Geometry for MGS occultation 8361M48A using the frame introduced in Figure 1. The X indicates the initial position of MGS and the adjacent curved black line indicates the path of MGS during the occultation, confirming that this is an ingress occultation. This line terminates at the point where MGS passed behind the solid surface of Mars as viewed from Earth. The two vertical grey lines indicate the ray paths between MGS and Earth at the start and end of the occultation. An arrow points towards Earth, whose r -coordinate is zero and whose z -coordinate is negative and very large.

1
2
3
4
5
6
7
8
9
10
11
12
13
14
15
16
17
18
19
20
21
22
23
24
25
26
27
28
29
30
31
32
33
34
35
36
37
38
39
40
41
42
43
44
45
46
47
48
49
50
51
52
53
54
55
56
57
58
59
60
61
62
63
64
65

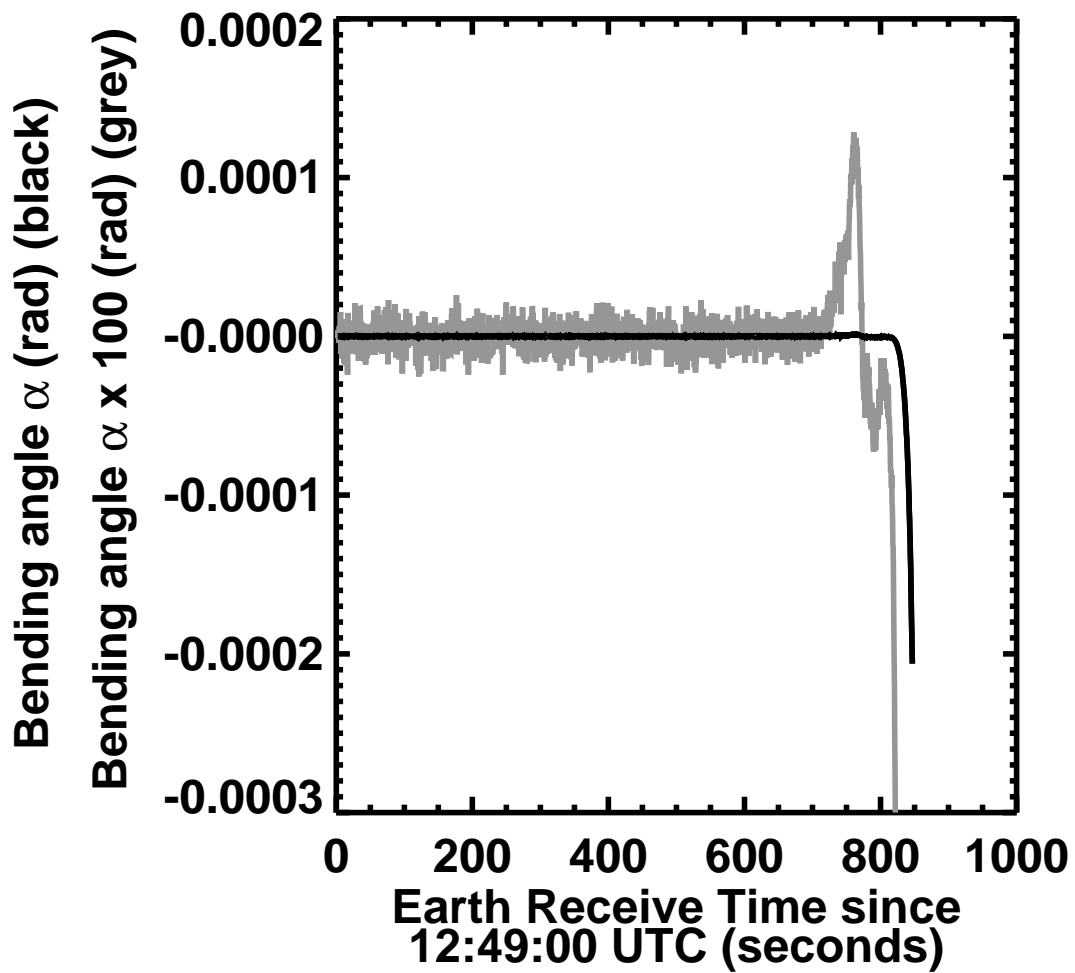


Fig. 4. Time series of bending angles α for MGS occultation 8361M48A. The black line shows original bending angles and the grey line shows $100 \times$ the bending angles, which highlights the positive bending angles caused by the ionosphere.

1
2
3
4
5
6
7
8
9
10
11
12
13
14
15
16
17
18
19
20
21
22
23
24
25
26
27
28
29
30
31
32
33
34
35
36
37
38
39
40
41
42
43
44
45
46
47
48
49
50
51
52
53
54
55
56
57
58
59
60
61
62
63
64
65

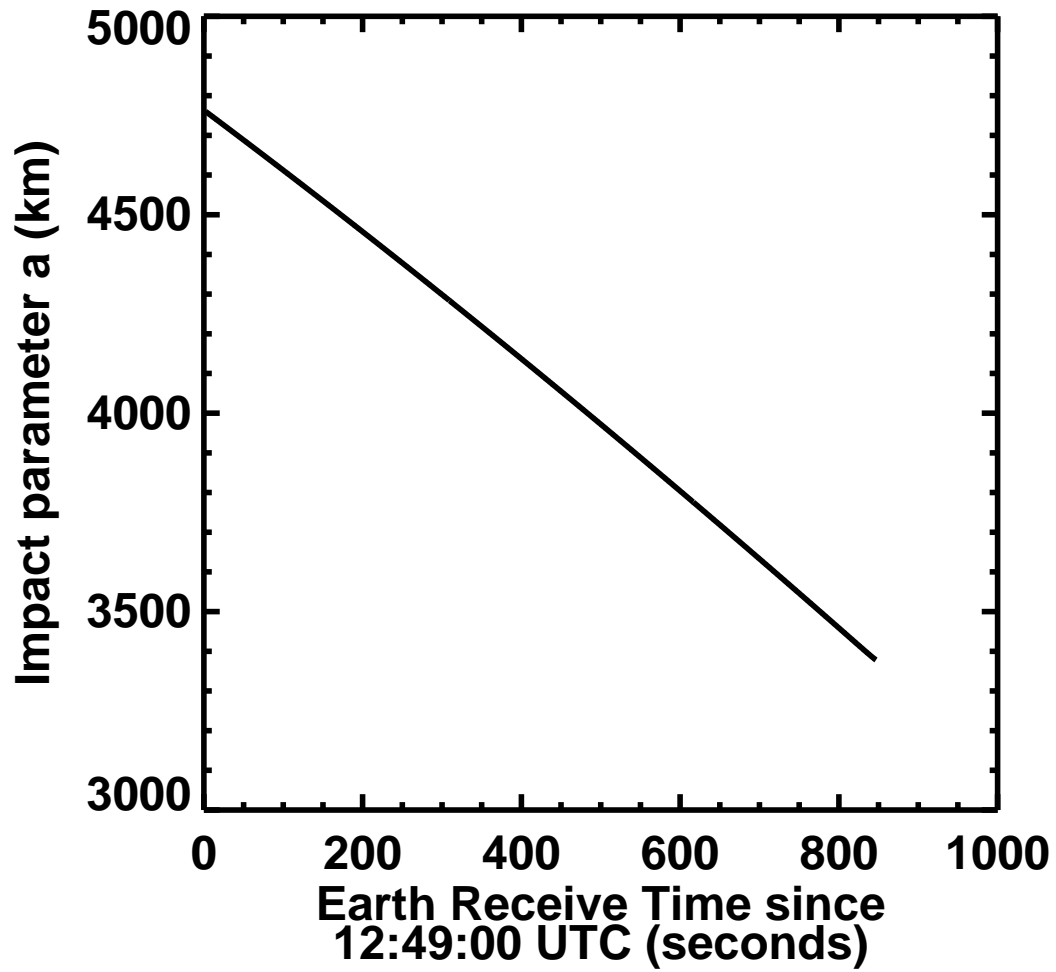


Fig. 5. Time series of impact parameters a for MGS occultation 8361M48A.

1
2
3
4
5
6
7
8
9
10
11
12
13
14
15
16
17
18
19
20
21
22
23
24
25
26
27
28
29
30
31
32
33
34
35
36
37
38
39
40
41
42
43
44
45
46
47
48
49
50
51
52
53
54
55
56
57
58
59
60
61
62
63
64
65

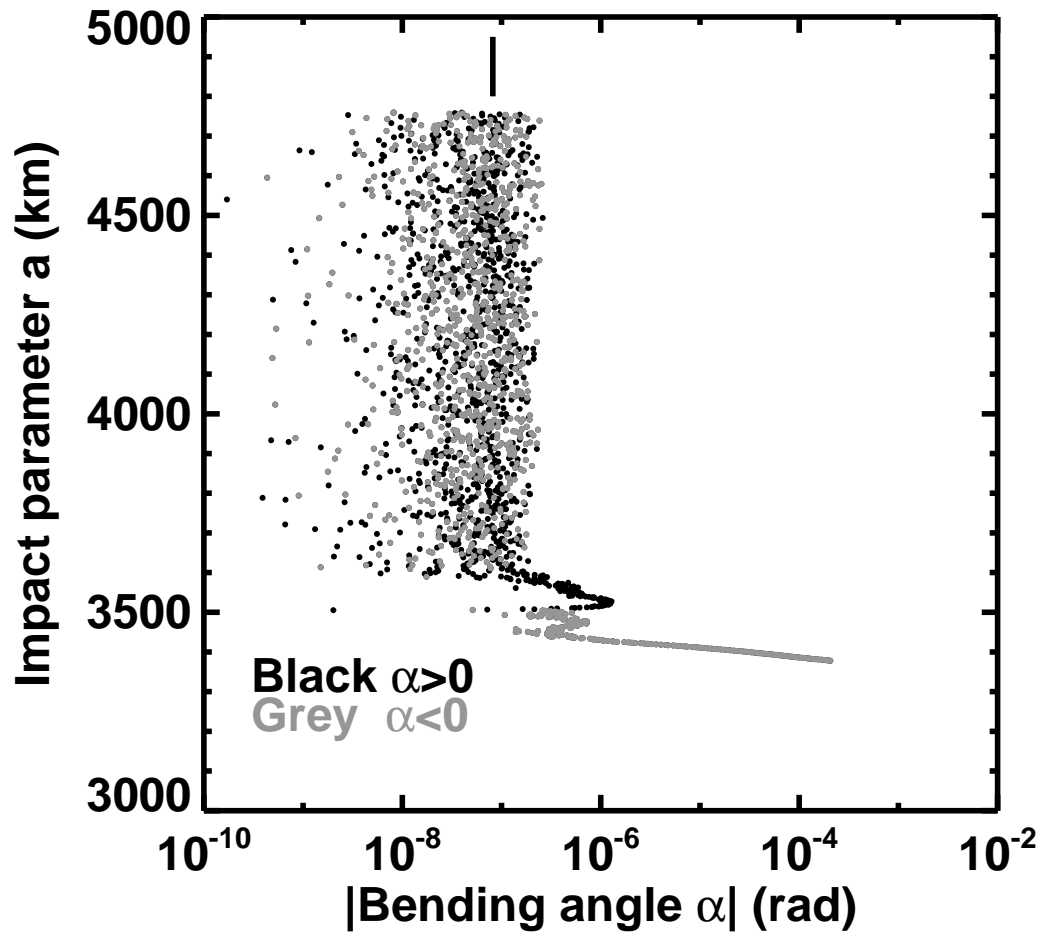


Fig. 6. Dependence of bending angle α on impact parameter a for MGS occultation 8361M48A. The absolute magnitude of each value of α is plotted, with black points indicating $\alpha > 0$ (the ionosphere) and grey points indicating $\alpha < 0$ (the neutral atmosphere). The salt-and-pepper values of α at high altitudes are caused by instrumental noise. The vertical line above the data points shows the standard deviation of the high altitude bending angles, 8×10^{-8} radians, and indicates the smallest measurable bending angle.

1
2
3
4
5
6
7
8
9
10
11
12
13
14
15
16
17
18
19
20
21
22
23
24
25
26
27
28
29
30
31
32
33
34
35
36
37
38
39
40
41
42
43
44
45
46
47
48
49
50
51
52
53
54
55
56
57
58
59
60
61
62
63
64
65

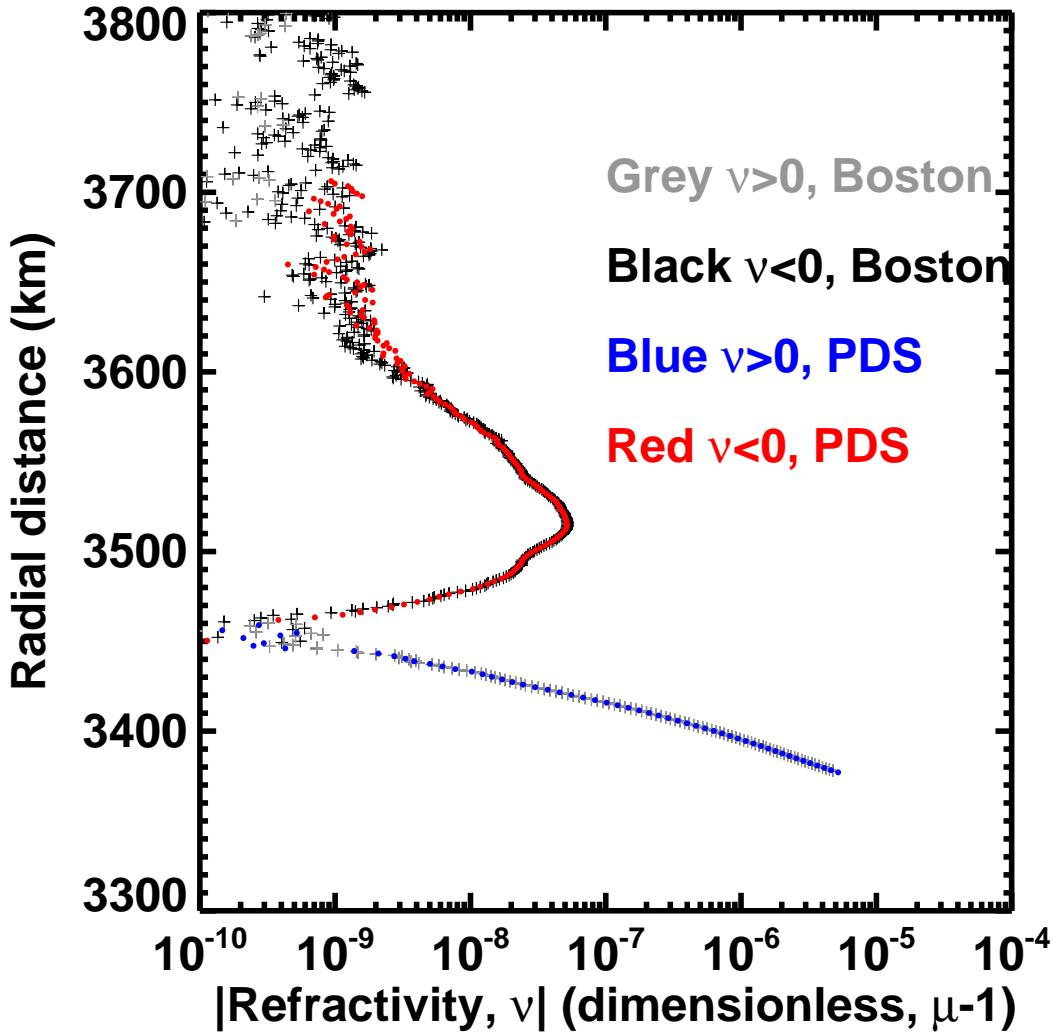


Fig. 7. Dependence of refractivity ν on radial distance R for MGS occultation 8361M48A. The absolute magnitude of each value of ν is plotted, with black crosses indicating $\nu < 0$ (the ionosphere) and grey crosses indicating $\nu > 0$ (the neutral atmosphere). Also plotted are refractivities associated with the archived profiles, with red points indicating $\nu < 0$ and blue points indicating $\nu > 0$.

1
2
3
4
5
6
7
8
9
10
11
12
13
14
15
16
17
18
19
20
21
22
23
24
25
26
27
28
29
30
31
32
33
34
35
36
37
38
39
40
41
42
43
44
45
46
47
48
49
50
51
52
53
54
55
56
57
58
59
60
61
62
63
64
65

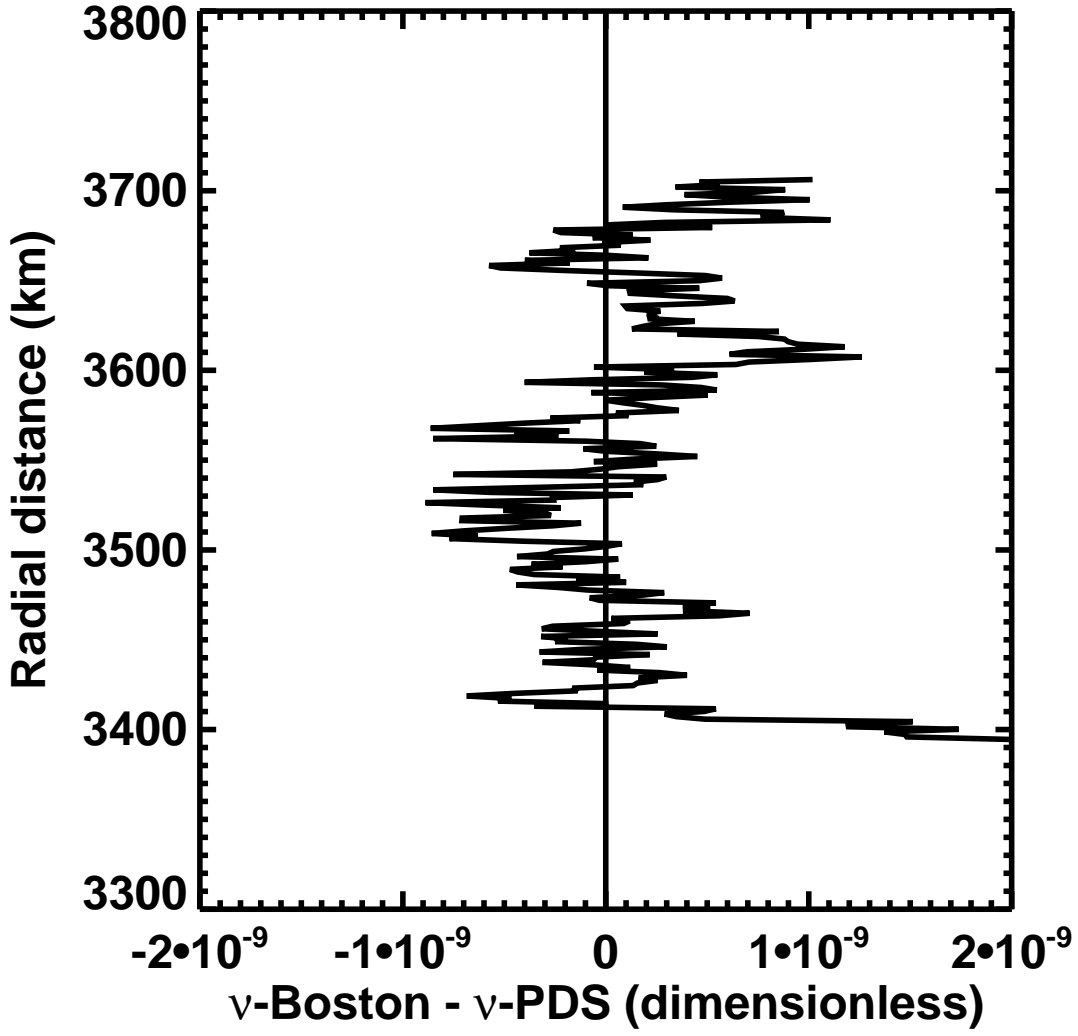


Fig. 8. Absolute difference between derived and archived refractivities for MGS occultation 8361M48A as a function of radial distance R . This emphasizes the ionospheric results as the absolute difference becomes relatively large at low altitudes.

1
2
3
4
5
6
7
8
9
10
11
12
13
14
15
16
17
18
19
20
21
22
23
24
25
26
27
28
29
30
31
32
33
34
35
36
37
38
39
40
41
42
43
44
45
46
47
48
49
50
51
52
53
54
55
56
57
58
59
60
61
62
63
64
65

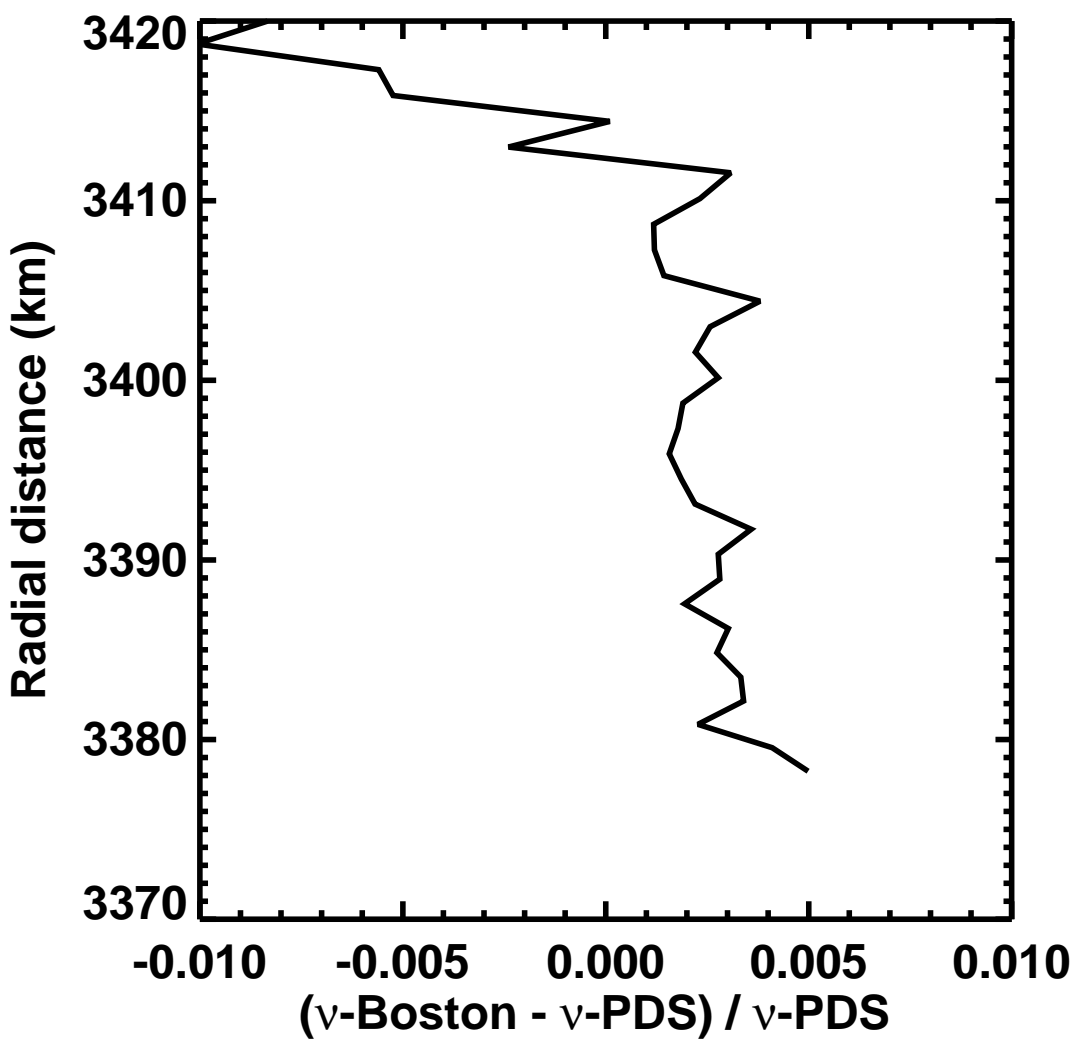


Fig. 9. Relative difference between derived and archived refractivities for MGS occultation 8361M48A as a function of radial distance R , with emphasis on the low altitudes neglected by Figure 8.

1
2
3
4
5
6
7
8
9
10
11
12
13
14
15
16
17
18
19
20
21
22
23
24
25
26
27
28
29
30
31
32
33
34
35
36
37
38
39
40
41
42
43
44
45
46
47
48
49
50
51
52
53
54
55
56
57
58
59
60
61
62
63
64
65

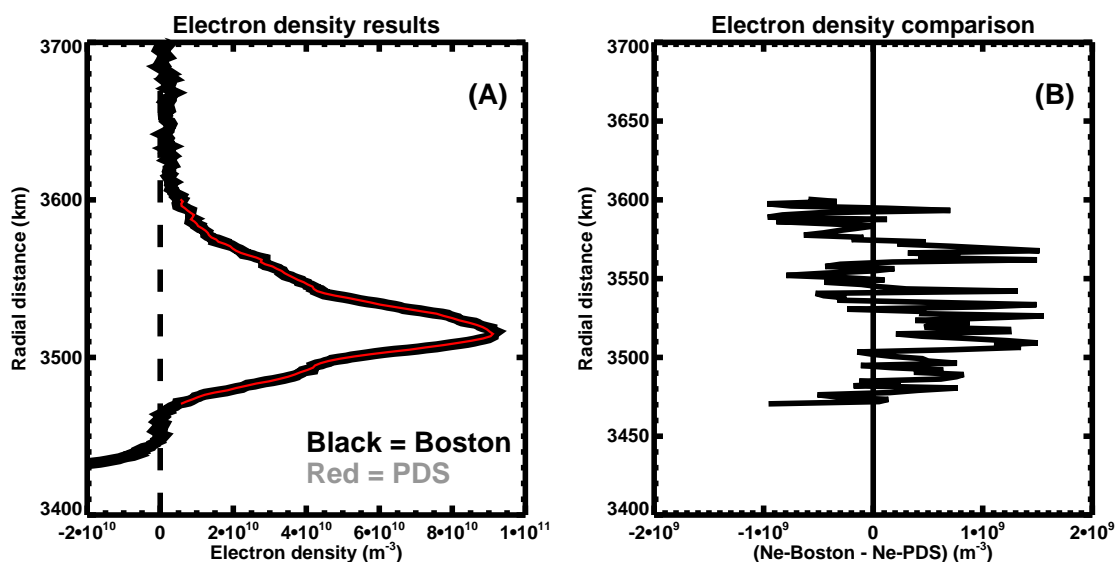


Fig. 10. A. Derived profile of ionospheric electron density for MGS occultation 8361M48A (black). Also shown is the corresponding archived profile (red). B. Comparison between the two profiles shown in Panel A, where Ne is electron density.

1
2
3
4
5
6
7
8
9
10
11
12
13
14
15
16
17
18
19
20
21
22
23
24
25
26
27
28
29
30
31
32
33
34
35
36
37
38
39
40
41
42
43
44
45
46
47
48
49
50
51
52
53
54
55
56
57
58
59
60
61
62
63
64
65

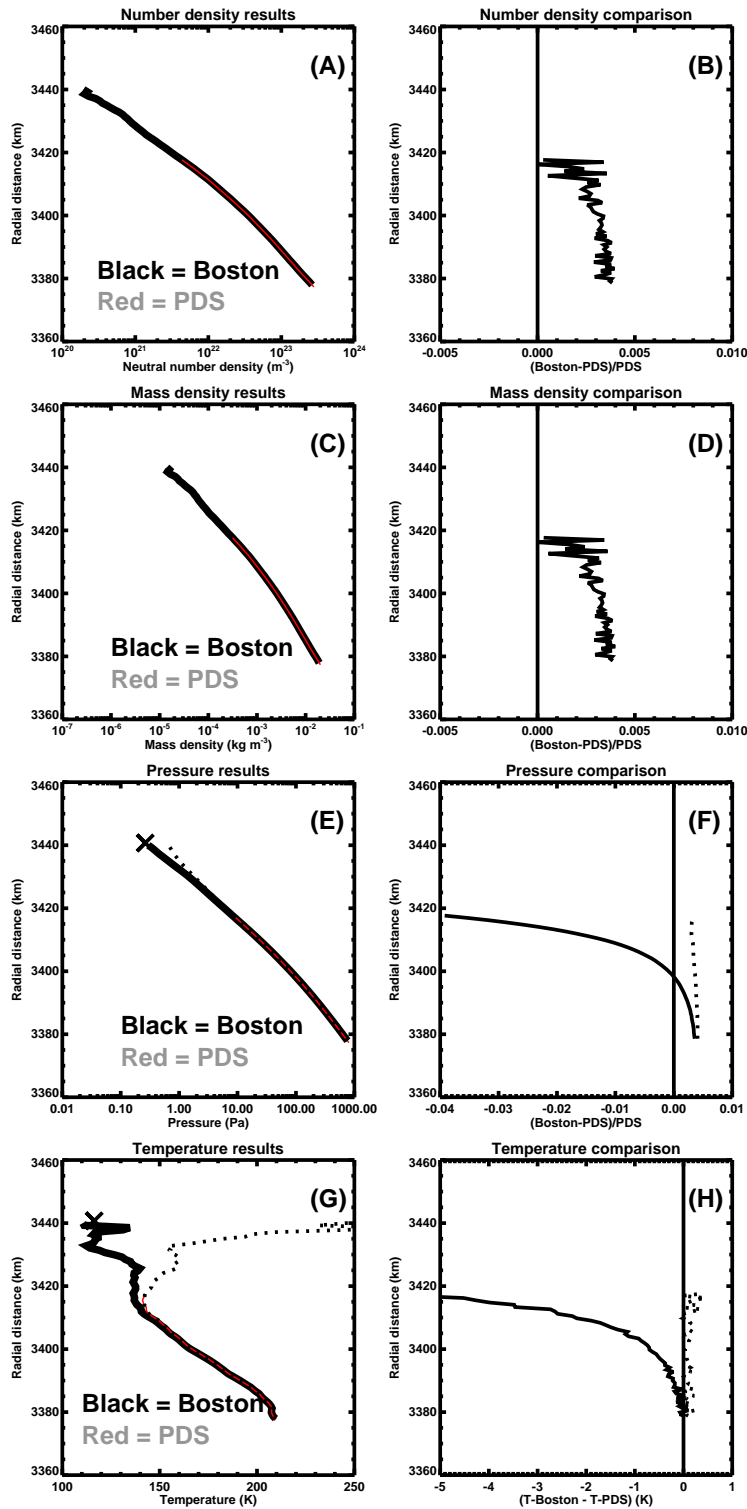


Fig. 11. A. Derived profile of neutral number density for MGS occultation 8361M48A (black). Also shown is the corresponding archived profile (red). B. Comparison between the two profiles shown in Panel A. Panels C and D are as panels A and B, but for neutral mass density. Panels E and F are as panels A and B, but for neutral pressure. Panels G and H are as panels A and B, but for neutral temperature. The X at 3440 km in Panels E and G highlights the imposed upper boundary conditions. Dotted lines in Panels E–H show profiles that use alternate upper boundary conditions, as discussed in the text.

Table 1

Conversions between symbols used in this work and in Fjeldbo et al. (1971).

Fjeldbo et al. (1971)	This work
f_s	$f_A(t_A)$
r_t^1	$r_B(t_B)$
z_t	$z_B(t_B)$
r_s	$r_A(t_A)$
z_s	$z_A(t_A)$
v_{rs}	$vr_A(t_A)$
v_{zs}	$vz_A(t_A)$
v_{rt}	$vr_B(t_B)$
v_{zt}	$vz_B(t_B)$
β_e	β_A
β_r	β_X
δ_s	δ_B
δ_r	δ_X
γ	γ

¹Symbol not explicitly used in Fjeldbo et al. (1971) since its value is by definition zero.